Materials & Design 268 (2026) 116546

Contents lists available at ScienceDirect

Materials & Design

journal homepage: www.elsevier.com/locate/matdes

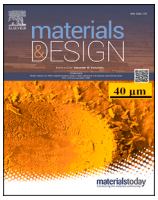

Development of a new high-strength diffusion-assisted healable Al-Mg-Zr alloy produced by Powder Bed Fusion - Laser Beam/Metals

Sophie De Raedemacker[a,*], Julie Gheysen[b], Florent Hannard[a], Julie Villanova[c], William Mottay[d], David Tingaud[e], Bartłomiej Winiarski[f], Masoud Ahmadi[a], Mohammed Farag[a], Hosni Idrissi[a], Khalid Hoummada[d], Moataz M. Attallah[g], Aude Simar[a,h]

[a] UCLouvain, iMMC (Institute of Mechanics, Materials and Civil Engineering), 1348, Louvain-la-Neuve, Belgium
[b] École Polytechnique Fédérale de Lausanne, 1015, Lausanne, Switzerland
[c] ESRF - The European Synchrotron, CS 40220, 38043, Grenoble Cedex 9, France
[d] Aix-Marseille Université, CNRS, IM2NP, 13397, Marseille, France
[e] Université Sorbonne Paris Nord, Laboratoire des Sciences des Procédés et des Matériaux, UPR 3407, CNRS, 93430 Villetaneuse, France
[f] Thermo Fisher Scientific, 627 00, Brno, Czech Republic
[g] Department of Materials, Loughborough University, Loughborough, LE11 3TU, UK
[h] WEL Research Institute, 1300, Wavre, Belgium

HIGHLIGHTS

- A healable, high-strength Al-Mg-Zr alloy is designed for additive manufacturing.
- Synchrotron X-ray nano-holo-tomography reveals healing of voids up to 3.7 μm.
- Hot isostatic pressing fully closes process-induced voids up to 100 μm.
- Zr addition doubles the yield strength compared to a reference Al-Mg alloy.

ARTICLE INFO

Keywords:
Aluminium alloy
Additive manufacturing
Self-healing
Synchrotron radiation
Tomography

ABSTRACT

Additive manufacturing enables complex lightweight aluminium components but often generates microvoids or microcracks degrading the mechanical properties. Introducing healing ability into high-strength Al alloys could mitigate these defects and improve structural integrity. A new high-strength and healable Al-Mg-Zr alloy, Almazium®, was developed and processed by Powder Bed Fusion - Laser Beam/Metals (PBF-LB/M). High Mg content and Zr-induced grain refinement produce a fine bimodal microstructure and a yield strength of 317 MPa in the as-built condition. Synchrotron X-ray nano-holo-tomography revealed that a Healing Heat Treatment (HHT) at 540 °C for 30 min fully closed 65 % of submicrometric voids, with complete healing up to 3.7 μm. At 400 °C, 90 % of submicrometric voids were fully healed, with a maximum healed size of 1.5 μm. Scanning Transmission Electron Microscopy and Atom Probe Tomography revealed a high Mg content in solid solution, supporting a Mg diffusion-based healing mechanism. The healing behaviour was maintained after a second thermal cycle, confirming the alloy's re-healability. Under combined heat and pressure, the healing efficiency increased drastically, allowing full closure of voids up to at least 100 μm. These findings demonstrate that Almazium® combines high mechanical strength with intrinsic, replicable healing ability.

1. Introduction

Aluminium alloys are of particular interest for aerospace and automotive industries due to their excellent strength-to-weight ratio [1]. Parts manufactured for those industries are often exposed to demanding service conditions, where repeated mechanical loads can lead to progressive structural degradation. In the context of developing a new

* Corresponding author.
Email address: sophie.deraedemacker@uclouvain.be (S. De Raedemacker).

https://doi.org/10.1016/j.matdes.2026.116546
Received 19 March 2026; Received in revised form 14 May 2026; Accepted 30 June 2026
Available online 2 July 2026

high-strength diffusion-assisted healable Al-Mg-Zr alloy produced by Powder Bed Fusion - Laser Beam/Metals (PBF-LB/M), the following section reviews the relevant state of the art in additive manufacturing of high-strength aluminium alloys and healing mechanisms in metallic systems.

1.1. PBF-LB/M of high-strength Al alloys

PBF-LB/M is increasingly used in aerospace and automotive industries due to its ability to produce lightweight parts with complex, topologically optimised geometries [1,2]. The main PBF-LB/M aluminium alloys used in industry are Al-Si and Al-Mg-Si alloys, with a composition close to eutectic (AlSi12). These have a lower strength than conventional high-strength wrought alloys (e.g., Al-Zn and Al-Cu alloys). High-strength Al alloys are difficult to produce by PBF-LB/M due to their hot cracking susceptibility [3,4]. Hot cracking can however be avoided by addition of a grain refiner element such as Sc and/or Zr [5–7] or Er [8], using a specific laser mode [9] or by preheating the substrate plate [10].

Al-Mg alloys are attractive due to their high weldability and good corrosion resistance [11]. However, Mauduit et al. [11] showed their sensitivity to hot cracking when processed by PBF-LB/M. Al-Mg alloys also present reduced mechanical properties compared to high-strength Al alloys. Furthermore, Mg could evaporate during manufacturing leading to turbulent melt pools, spatters and pores, reducing the density and surface quality of the manufactured part [12–14]. Although an Al-Mg alloy with high Mg content has been successfully processed by PBF-LB/M, its strength (132 MPa) remains insufficient to compete with conventional high-strength alloys [15–17].

Ti/TiB_2 is a grain refiner widely reported in the literature of Al alloys, exhibiting strong grain-refining capability due to its low lattice mismatch with Al [18,19]. However, Ti is not known to form hardening precipitates, which limits its hardening potential [20,21]. Sc is another known hardening element for Al-Mg alloys (e.g., Scalmalloy® [22,23]) but its scarcity, motivates the use of Zr as an alternative grain refiner and strengthening element in PBF-LB/M Al alloys. Zhang et al. [6] showed that adding 2 wt% of Zr to an Al–Cu–Mg alloy reduced hot cracking and increased the yield strength from 253 MPa to 446 MPa. The optimal Zr content addition was studied for an Al-4.24Cu-1.97Mg-0.56Mn alloy by Nie et al. [24]. They observed that 2 wt% allowed to reach a higher density, regardless of manufacturing parameters used. 2 wt% was also the optimal content to reach a higher yield strength (464 MPa) and ultimate tensile strength (493 MPa). In another study, Martin et al. coated 7075 and 6061 powders with ZrH_2 [25]. With this coating, parts without any hot cracking were manufactured by PBF-LB/M for both kinds of powders. Primary Al_3Zr precipitates acted as heterogeneous nucleation sites for the growth of small equiaxed grains. In their studies, Nothomb et al. confirmed that the addition of ZrH_2 allowed to avoid hot cracking in 7075 alloy [13,14].

Zr has also shown promising effects in Al-Mg alloys. Zhou et al. investigated AA5083 with and without Zr addition [26] and reported that Zr significantly improved printability, reducing crack density by at least half under identical processing conditions. In addition, Zr enhanced the mechanical response: the as-built (AB) AA5083 + Zr exhibited a yield strength of ~212 MPa, compared with 145 MPa for annealed AA5083. Zhou et al. also studied the impact of different heat treatments on the hardness of AA5083 + Zr. The addition of Zr enabled age hardening in this Al-Mg alloy while these alloys are usually known to be non-age-hardenable due to the difficulty in controlling the growth of Al-Mg precipitates [27]. Another example of an Al-Mg alloy with addition of Zr is the Addalloy®. Croteau et al. manufactured this alloy by PBF-LB/M and obtained parts with a density of 99.2 % and no cracks [28]. The average tensile strength obtained for AB Addalloy® was 290 MPa while it increased up to 365 MPa after peak-aging.

1.2. Healable alloys

In components produced by PBF-LB/M, structural degradation is typically initiated at intrinsic process-induced defects. Three main types of defects are usually observed after manufacturing in PBF-LB/M parts [29]: (i) gas pores, generally spherical and smaller than 5 μm; (ii) keyhole pores, also spherical but larger (30–150 μm) due to excessive laser energy; (iii) lack-of-fusion defects, irregular voids that can reach several hundred micrometers when energy input is insufficient. These defects serve as preferential crack-initiation sites under cyclic loading [30,31]. Instead of discarding damaged parts, replacing them or delaying crack formation, an alternative strategy is to explore so-called “self-healing” mechanisms, which could extend the service life of additively manufactured components. A healable material is a material able to heal its own cracks or voids. One of the most widely developed healable artificial materials is polymers [32,33], whose chemical reactions create sufficient energy to re-establish secondary bonds and in which diffusion is easily possible even at room temperature.

Metal healing is more challenging, given the low diffusion capacity of atoms at room temperature [34] and the high energy of metal bonds. Two categories of healable metals are distinguished [33,35]. First, microscopic metal systems rely on the diffusion of healing agents (i.e., metal atoms) to fill microcracks at low or high temperatures [35,36]. Arseenko et al. proposed a Programmed Damage and Repair (PDR) for a diffusion-healable Al-Mg-Si alloy [37]. The method introduces particles localising damage, directing void formation to these sites. When loading is interrupted, a Healing Heat Treatment (HHT) enables atomic diffusion to close the voids, with conditions chosen to limit microstructural changes and preserve strength. After damage and heat treatment at 400 °C for 10 min, synchrotron X-ray nano-holo-tomography (X-ray nano-CT) revealed that 90 % of damage smaller than 0.2 μm was healed. Solid-state diffusion has also been demonstrated as an effective healing mechanism in an Al–Mg–Er alloy [38]. Annealing at 180 °C enables Mg to first diffuse into voids located between Al_6Mn precipitates, leading to their complete closure. With sufficiently long treatment times, Al diffusion further contributes to homogenising the microstructure. However, this mechanism is inherently limited to nanoscale voids, and the much larger pores generated by the PBF-LB/M process (several tens of μm) lie well beyond the healing capability of solid-state diffusion.

The second category of healable metals are macroscopic metal systems, able to heal voids similar in size to these pores. Among these, liquid-based healing strategies rely on a heat treatment to melt the healing agent, allowing it to reach the damaged area before solidifying [35]. A possibility for liquid-based systems is to use a low melting point eutectic phase as healing agent. By applying a heat treatment at a temperature between the eutectic temperature and the melting temperature of the matrix, the eutectic phase will become liquid and will be able to heal the damaged areas [31,35,39,40]. Gheysen et al. produced by PBF-LB/M a low-strength healable AlMg8 alloy where the eutectic phase (Al_3Mg_2) forms an interconnected network surrounding the α-Al matrix [16]. After HHT at 540 °C for 30 min, X-ray nano-CT revealed that 95 % of voids were healed, and a considerable number of pores smaller than 2 μm were completely healed without any deformation or loss of structural strength of the part. The addition of pressure further enhanced healing effectiveness. After Hot Isostatic Pressing (HIP) at 540 °C and 300 MPa for 30 min on AlMg8, almost no pores were observed (porosity = 0.008 %) and a void with a diameter of 80 μm was healed [15]. The HIP treatment also allowed improving the static and fatigue properties of this alloy. However, in this case, distortion of the part was observed and open pores were not healed. Hu et al. also studied the application of pressure to improve healing for an IN738LC alloy [41]. They first heated under vacuum the part up to a temperature where melting at grain boundaries was obtained. Once around 10 vol% of liquid was

reached, an isostatic pressure of 5 MPa was applied. The part was finally cooled down in a controlled fashion under isostatic pressure. All cracks were healed with this strategy while few microvoids were still present.

1.3. Goal of this work

While previous studies have shown that Mg diffusion can facilitate void and crack healing in Al-based alloys, these investigations have predominantly focused on age-hardenable systems, such as Al–Cu–Mg or Al–Mg–Si alloys, particularly in the underaged state where solute atoms remain largely in supersaturated solid solution, providing substantial healing potential. In contrast, conventional Al–Mg alloys are generally non-age-hardenable and contain moderate Mg levels, particularly in solid solution, which limits both their mechanical strength and healing ability. The Al–Mg alloy studied here is distinguished by its high Mg content in the raw material and in solid solution due to the rapid cooling inherent to PBF-LB/M which enhances diffusion-driven healing, while the addition of Zr promotes grain refinement, avoiding hot cracking during PBF-LB/M, and significant strengthening relative to previously studied healable AlMg8 [15,16]. This combination has enabled the development of an alloy manufactured by PBF-LB/M, Almazium®. The novelty of the Almazium® alloy is that it is simultaneously high-strength and healable. Healing in this alloy was demonstrated using X-ray nano-CT during both HHT and Healing Heat and Pressure Treatment (HHPT), and its mechanical properties were evaluated AB and after various HHT conditions.

2. Materials and methods

2.1. Alloy design criteria

In diffusion-based healing strategies, several criteria must be considered when selecting a suitable healing agent [34,38,42]: i) the presence of a supersaturated solid solution, ii) a diffusion coefficient of the healing agent higher than the self-diffusion coefficient of the matrix, iii) a preferential precipitation of the healing agent on free surfaces or voids rather than within the matrix. Based on those criteria, Mg appears to be a promising candidate. The rapid cooling rates inherent to PBF-LB/M technology (10^6 K/s [5]) enable trapping of Mg atoms in supersaturated solid solution, making this manufacturing process particularly suitable. Furthermore, Mg exhibits a high diffusion coefficient in Al [43] and a maximum solubility of approximately 17 wt% at 450 °C [44]. Zhang et al. [45] demonstrated that larger solute atoms increase the strain energy, thereby raising the energy barrier for homogeneous nucleation in the matrix. As a result, solute atoms remain available for heterogeneous precipitation on voids and free surfaces where they can contribute to void filling. Mg atoms are approximately 16 % larger than Al atoms [46], which further supports its suitability as healing agent. Consistently, Mg is known to precipitate heterogeneously on defects [47] rather than homogeneously within the matrix. To mitigate hot cracking, the Mg content after manufacturing should exceed 4 wt% [11]. A composition of approximately 8 wt% was targeted in order to enable comparison with AlMg8.

To obtain a high-strength alloy, Zr was selected as a strengthening alloying element due to its well-documented ability to refine the microstructure, thereby enhancing mechanical properties and reducing hot cracking susceptibility, as well as promoting the formation of coherent $L1_2$ Al_3Zr strengthening precipitates [28]. Zr addition also helps to improve resistance to grain coarsening [48] during heat treatment. Finally, no Mg-Zr intermetallic phases are expected to form under the investigated conditions according to Thermo-Calc simulations (see Supplementary A). Mg in solid solution is thus not consumed through reactions with Zr, and remains available as healing agent.

2.2. Raw material and sample manufacturing

The Almazium® powder is obtained by mechanically mixing for 3 hours in a Turbula (Willy A. Bachofen AG, Switzerland) 14 wt% of 99.8 % pure Mg powder (SFM, Switzerland) with 2 wt% of 99.48 % pure Zr 702 powder (TLS Technik, Germany) and the balance of 99.7 % pure Al powder (TLS Technik, Germany). Powder mixing was performed in ambient air, without the use of a protective atmosphere. Partial surface oxidation of Mg during powder handling cannot be excluded. The composition is then verified by Inductively Coupled Plasma (ICP) (see Table 1). The powder particle size distribution was measured using a SYNC particle analyser (Microtrac, USA), yielding a mean particle diameter of 42 ± 15 µm. The particle size distribution of the raw powder and Scanning Electron Microscope (SEM) images of the powder mixture, illustrating particle morphology and size heterogeneity, are provided in Supplementary B. The parts were manufactured in a ProX DMP 200 PBF-LB/M machine (3D Systems, USA). In this work, samples were manufactured with a laser power of 191 W, a scanning speed of 300 mm/s and a hatch spacing of 60 µm. These parameters were chosen based on a parameter optimisation study aiming to maximise the relative density of parts. The full optimisation procedure is detailed in Supplementary C. The average composition of the AB parts is measured by ICP and provided in Table 1. A Mg loss of 52 % is evidenced between the powder mix and the AB part, which justifies the use of 14 wt% Mg in the initial powder in order to achieve a final Mg content of approximately 8 wt% after processing. This Mg evaporation reduces the overall Mg content of the alloy and may consequently decrease the healing potential and solid solution strengthening. The impact on the maximum healable defect size is discussed in Section 3.1. Several approaches have been proposed to mitigate Mg vaporisation during processing. These include the use of He as a shielding gas and increasing its pressure to raise the boiling point of Mg [49], optimising the gas flow to effectively remove vaporisation by-products while avoiding disturbance of the powder bed [50], removing the smallest and largest powder particles from the feedstock [50], and adding small amounts of Ca, which has been shown to reduce Mg evaporation in Scalmalloy® without compromising mechanical properties [51]. The use of a pre-alloyed powder is also expected to mitigate Mg evaporation, but was not considered in the present proof-of-concept study. Although increasing Mg content could compensate for Mg losses during PBF-LB/M and improve healing, the alloy investigated here already contains a relatively high Mg level. Additional Mg additions would promote a higher fraction and continuity of the β-Al_3Mg_2 phase at grain boundaries, increasing corrosion susceptibility [52]. Mg-rich eutectic phases are also brittle and can act as crack-initiation paths, potentially degrading mechanical reliability and printability [16]. The selected Mg content therefore represents a compromise between healing potential, mechanical properties, manufacturability, and corrosion resistance. Further composition optimisation remains a challenge for future alloy design.

Table 1
ICP measurement performed on the Almazium® powder mix and on a PBF-LB/M sample processed with the optimised set of parameters.

	[wt%]	Al	Mg	Zr	Fe	Si	Cu	Ga	Mn	Ti
Powder	*Mean*	bal	13.91	1.87	0.11	0.04	0.02	0.01	0.01	0.01
	St. Dev.	–	0.16	0.06	0.01	0.02	0.00	0.00	0.00	0.00
PBF-LB/M sample	*Mean*	bal	6.72	2.39	0.12	0.03	0.03	0.01	0.01	0.01
	St. Dev.	–	0.17	0.07	0.00	0.01	0.00	0.00	0.00	0.00

2.3. Microstructural analysis

The samples were sectioned along the building direction before being embedded in a carbon-filled conductive hot-coating resin Escil GEPD/Ca (Escil, France). Microstructure has been analysed by SEM with an Ultra 55 (Zeiss, Germany). Chemical analysis by Energy Dispersive X-ray Spectroscopy (EDS) have also been undertaken with an AXS XFlash 5010 (Bruker, USA). Electron backscatter diffraction (EBSD) analysis was performed to assess changes in grain size and orientation after the

samples were subjected to a HHT. The measurements were performed using an Apreo 2S field emission scanning electron microscope (FE-SEM) (Thermo Scientific, USA), equipped with a Symmetry detector (Oxford Instruments, UK), and operated using Aztec software (Oxford Instruments, UK). The microscope was operated at an accelerating voltage of 20 kV, a probe current of 15–20 nA (optimised for EBSD indexing acquisition) and a working distance of 10–15 mm (depending on the sample geometry). EBSD patterns were acquired with a step size of 0.204 μm for lower magnification maps and 0.08 μm for higher magnification maps over areas of $209 \times 144\ \mu m^2$ and $64 \times 44\ \mu m^2$, respectively, with a sample tilt of 70° relative to the incident electron beam. The subsequent data processing was conducted utilizing ATEX software (ATEX, France) for the purpose of grain boundary mapping and crystallographic orientation analysis [53]. The inverse pole figure (IPF) maps were plotted with respect to the build direction of the samples, corresponding to the Y direction of the SEM coordinates system.

Scanning Transmission Electron Microscopy Energy-Dispersive X-ray Spectroscopy (STEM/EDX) was performed on a Talos microscope (Thermo Scientific, USA), operating at 200 kV. The STEM/EDX images and spectra were acquired in scanning mode with a beam intensity of 200 pA, using a 70 μm condenser aperture and a spot size of 7.

Atom Probe Tomography (APT) was used to investigate the solid solution of AB and HHT samples. Analyses were performed at 40 K, 30 pJ laser energy and 0.5 % evaporation rate on a LEAP 3000 X-HR (CAMECA, France) with a 37 % detection rate. APT tips were prepared by focused ion beam (FIB) using a dual beam SEM/FIB Helios NanoLab 600 (Thermo Scientific, USA) using the standard lift-out procedure [54], consisting of a three steps annular milling at 30 kV and two cleaning steps at 5 kV and 2 kV. APT data were processed using the IVAS software (CAMECA, France).

2.4. Characterisation of the healing capacity

Differential scanning calorimetry (DSC) STA 449 F3 Jupiter (Netzsch, Germany) was used to determine the temperature of HHT based on the solidus temperature of Almazium®. The heating program initially consisted of a heating rate of 50 °C/min up to 700 °C followed by cooling to room temperature at the same rate (50 °C/min). This heating rate was selected to better approximate the rapid temperature increase experienced by small specimens when introduced into a preheated furnace during HHT. To assess possible thermal lag effects, additional DSC measurements were conducted at a lower heating rate of 10 °C/min (see Supplementary D). No significant difference in the measured solidus temperature was observed between the two heating rates, indicating that thermal lag does not significantly affect the determination of the solidus for Almazium®. For both measurements, the reference was an empty graphite crucible, while the sample was placed in a separate graphite crucible. Both crucibles were sealed with graphite lids. Argon was used as shielding gas.

Thermo-Calc [55] version 2024b with TCAL8 Al-alloys v8.2 database was used to predict the solid solution composition at room temperature and the solidus temperature of Almazium®.

To study the healing capacity of Almazium® through the evolution of porosity before and after HHT, synchrotron X-ray nano-CT was performed at beamline ID16B of the European Synchrotron Radiation Facility (ESRF, Grenoble, France) [56]. This experiment allows acquiring high resolution (HR) images (voxel size of 35 nm) by using an X-ray beam with a high energy of 29.6 keV. Some scans with a low resolution (LR) (voxel size of 241 nm) were also acquired to obtain a larger field of view of the samples and capture the largest voids. For each scan, 3203 projections were taken with an acquisition time of 0.05 s per projection. To apply a HHT, a furnace was used as the sample environment on the experimental set-up. The *in-situ* heating capabilities of ID16B allow applying the HHT on the sample without removing it from the nano-CT stage i.e., scanning the exact same location before and after HHT. The furnace can be moved up and down above the sample for fast heating or cooling. It can also be controlled in ramp temperatures for slow heating and cooling. After HHT, samples were cooled down to 400 °C at 10 °C/min to avoid to generate cracks which could possibly appeared during a fast cooling.

To study the healing through a HHPT, samples were sent to the Université Sorbonne Paris Nord (Villetaneuse, France) to be treated in a HIP facility. The treatment was performed at 540 °C for 30 min under a pressure of 300 MPa. The heating and cooling ramps were both 10 °C/min. Argon was used as an inert gas to apply pressure.

Two kinds of samples were studied at ESRF: damaged and AB ones. Damaged samples were extracted just below the fracture surface of tensile samples (see Fig. 1a) while AB samples were extracted in bulk cubes. In both cases, samples were manually thinned down to 300 μm and then cut with a micro-cutting machine Accutom-5 (Struers, Denmark) to obtain final parts with a cross section of $300 \times 300\ \mu m^2$. Once the samples were cut, they were mounted on alumina tubes (outer diameter = 1.5 mm and inner diameter = 0.8 mm) (Sceram, France) with a cement paste Resbond 940HT (Polytec PT, Germany). Those tubes were then mounted on brass pins. Finally, for samples requiring an inert atmosphere during heat treatment, a quartz glass capsule (length = 46 mm, outer diameter = 2 mm and wall thickness = 0.01 mm) (Hilgenberg, Germany) was mounted under Ar atmosphere and sealed with cement. The final mounting is depicted in Fig. 1a.

Data obtained were finally reconstructed with an ESRF in-house phase retrieval code using a δ/β of 528 and PyHST2 software with filtered back-projection reconstruction [57]. A manual registration of volumes before and after HHT was first done. Filtering and segmentation methods used for all samples are described in Supplementary E. After void detection by segmentation, the barycenters of each void before and after HHT were retrieved. Then tracking of voids was performed to compare the evolution of their volume before and after healing. This tracking was made with a Matlab code (MathWorks, USA) by identifying, for each void after healing, the corresponding void before healing through minimisation of the Euclidean distance between their barycenters. This position-based criterion was chosen because the healing process strongly modifies void size and morphology, making shape-based descriptors unreliable for tracking. Nevertheless, this approach has some limitations: void coalescence or fragmentation may break the one-to-one matching assumption, significant morphology changes may shift barycenter positions and introduce matching errors, and although the two volumes were manually aligned as carefully as possible prior to analysis, a small residual misalignment may remain and contribute to uncertainty in the matching procedure. To mitigate these limitations, all automatically obtained correspondences were systematically verified. The parameter dV was then defined as follows:

$$dV = \frac{V_{after} - V_{before}}{V_{before}} \cdot 100 \qquad [\%] \tag{1}$$

V_{after} is the volume of the void after healing [μm^3] and V_{before} is the volume of the same void before healing [μm^3]. This means that if dV is negative, the volume of the void is reduced during healing and is totally healed when $dV = -100\,\%$. When a void detected after HHT had no corresponding feature in the pre-HHT dataset, it was manually inspected. These cases were determined to result from segmentation errors rather than the formation of new voids during HHT.

X-ray laboratory tomography with an Easytom S equipment (RX Solutions, France) was also used to study the healing ability of Almazium® after HHPT. The parameters used were a voxel size of 5 μm, a current of 34 μA and a voltage of 117 kV.

Other methods used to study the healing ability of Almazium® are multi-scale correlative tomography and multi-modal electron microscopy already used in different studies on Al-Mg alloys [58,59]. The concept is to study a sample with different techniques and at different scales to identify an interesting zone and then analyse it in more details at a higher scale, see Fig. 1. In order to capture nano-scale details of the internal microstructure, samples were first scanned at ESRF by

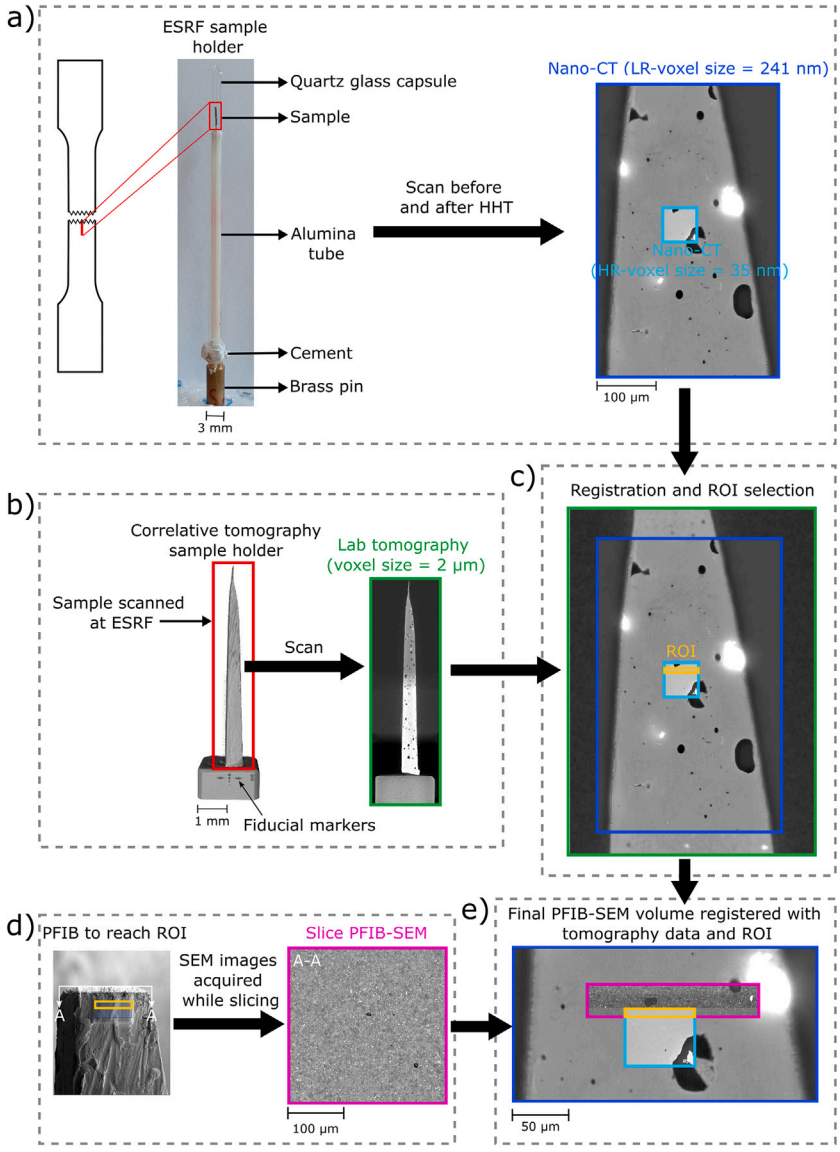

Fig. 1. Principle of the multi-scale correlative tomography and multi-modal electron microscopy performed on the ESRF nano-CT sample. a) In red, position where pre-damaged samples for synchrotron X-ray nano-CT (HR-voxel size = 35 nm in turquoise and LR-voxel size = 241 nm in blue) were extracted just below the fracture surface of tensile samples and the assembly of those samples on ESRF sample holder. Those samples were scanned before and after HHT each time by nano-CT (HR and LR). b) Recovery of the sample on the ESRF sample holder and mounting on correlative tomography holder with fiducial markers. The sample is then scanned with laboratory tomography (voxel size = 2 µm). c) Registration of nano-CT (HR and LR) and laboratory tomography and selection of a ROI. d) Use of PFIB to reach the borders of the ROI before acquisition of SEM images every 50 nm. e) Final registered volume with nano-CT (HR and LR), PFIB-SEM volume and ROI. (For interpretation of the references to colour in this figure legend, the reader is referred to the web version of this article.)

X-ray nano-CT (HR-voxel size = 35 nm and LR-voxel size = 241 nm) as described earlier, see turquoise and blue boxes respectively in Fig. 1a. The sample was then retrieved from the assembly shown in Fig. 1a and mounted on a specific correlative tomography holder containing fiducial markers (see Fig. 1b). Subsequently, the sample on the correlative holder was scanned by a laboratory tomograph Easytom S (RX Solutions, France) (green box in Fig. 1b). The parameters used were a voxel size of 2 µm, a current of 64 µA and a voltage of 100 kV. Tomography scans obtained at the three scales were finally registered together using Avizo 3D software to enable the accurate localisation of a Region Of Interest (ROI) (orange box in Fig. 1c). By comparing nano-CT scans obtained before and after HHT, it was possible to select a specific ROI where voids were completely healed to confirm their complete healing, as well as confirm that they are not just smaller than the detection limit of nano-CT. Based on the registration of images, the borders of that selected ROI was reached by using Plasma Focused Ion Beam - Scanning Electron Microscope (PFIB-SEM) in a DualBeam Thermo Scientific Helios Hydra (Thermo Scientific, USA) (see Fig. 1d). Coregistration of the nano-CT data with the PFIB-SEM stage coordinate system was performed using a holder/adapter kit and the Thermo Scientific Maps Correlative software (Thermo Scientific, USA). Auto Slice and View 5 (Thermo Scientific, USA), an automated PFIB serial sectioning tomography, was later applied to reach the selected ROI. This technique uses a Xe beam at 30 keV and 60 nA with 3° rocking polish and creates slices with a thickness of 25 nm. Backscattered electrons SEM images were collected every second slice using a beam of 5 keV and 1.6 nA and a CBS detector with a dwell time of 3 µs and a pixel size of 25 nm (see Fig. 1d). The final volume obtained has a voxel size of $25 \times 25 \times 50\,nm^3$. On the same DualBeam EDS maps, line scans and point analyses were collected by an Aztec 4 (Oxford Instruments, UK) and X-Max 50 detector (Oxford Instruments,

UK), with an energy of 20 keV and a current of 1.6 nA, on the ROIs of the healed zones. The final PFIB-SEM volume was finally registered with HR and LR nano-CT and the ROI (see Fig. 1e).

2.5. Mechanical properties

Tensile tests were performed with a Zwick/Roell 50 kN (Germany). The gauge length was 20 mm, and the displacement of the crosshead was set at 1 mm/min. Tensile samples were machined from plates with dimensions $100 \times 13 \times 1.5\,mm^3$ manufactured perpendicular to the building direction. The machining was done by Electrical Discharge Machining (EDM) and followed the ASTM-E8M standard with a thickness of 1.5 mm, a reduced section length of 26 mm and a reduced section width of 6 mm (see Fig. F.1 in Supplementary F). Different HHTs were applied on tensile samples in an Ar atmosphere with a Nabertherm L9/11 (Germany). Isothermal HHTs at 540 °C were performed for 1, 3, 5, 10, 20 and 30 min. This temperature was selected because it was the highest one tested for HHT and because previous studies have shown that, above 500 °C, the hardness of Al–Zr alloys decreases. Therefore, 540 °C was considered to represent the worst-case scenario [60]. The effect of the HHT temperature was also tested with isochronal treatments of 30 min at 400 °C, 460 °C, 480 °C, 520 °C and 540 °C. For each condition, once the furnace reached the target temperature, the sample was placed inside for the desired time. At the end of the treatment time, the sample was cooled down with a rate of 10 °C/min up to 400 °C then removed from the furnace so that they were submitted to the same conditions as the samples tested at ESRF. Before performing the tensile test, samples were polished with SiC paper (80, 320 and 1200 grid size) in order to remove their surface roughness.

To compare Almazium® with the previously studied AlMg8 alloy [15,16], the specimen geometry, build orientation, post-processing, testing methodology, and data treatment were kept identical. The only differences lie in the PBF-LB/M processing parameters, which were optimised separately for each alloy. Consequently, the final Mg content differs between the two materials due to distinct evaporation behavior during processing. Almazium® contains 6.7 wt% of Mg, whereas AlMg8 contains 8.4 wt% of Mg. This difference is explicitly considered in the strengthening analysis presented in Section 3.4.

3. Results and discussion

3.1. Microstructure before and after HHT

Considering the high cooling rates experienced during PBF-LB/M manufacturing (10^6 K/s [5]), the final microstructure obtained will not be the one predicted by the equilibrium phase diagram, i.e., grains of α-Al with around 1.5 wt% of Mg in solid solution and some $\beta - Al_3Mg_2$ precipitates at the grain boundaries [44]. Fig. 2 displays SEM backscattered electron images of the AB microstructure of Almazium® produced by PBF-LB/M. In Fig. 2a, different shades of grey are noticeable, indicating heterogeneities in the composition of the microstructure. Fig. 2a exhibits, a large white particle (circled), identified by EDS as unmelted Zr (see Fig. G.1 and Table G.1 in Supplementary G). It corresponds to a processing artefact. Indeed, Zr has a high melting point (1855 °C) and all Zr particles cannot be melted during manufacturing. Such kind of unmelted Zr particles have also been reported by Larini et al. [61]. They demonstrated that large unmelted Zr particles do not have any significant effect on local microstructural refinement. Instead, grain size reduction is primarily governed by the formation of Al_3Zr (between 100 nm and 400 nm [62]) precipitates and the local solidification rate. In the present study, EBSD observations are consistent with this interpretation (see Fig. 3). The size difference between the coarse unmelted Zr particles and the much finer grains formed during PBF-LB/M (in the micrometer range, see Fig. 3a) makes a dominant heterogeneous nucleation role of these particles unlikely. The use of a pre-alloyed powder should allow mitigating the presence of these artefacts. This is a future prospect of this alloy design but was not considered in the present proof-of-concept alloy. Fig. 2b shows a higher magnification micrograph. Some primary Al_3Zr precipitates, confirmed by EDS analysis (see Fig. G.2 and Table G.2 in Supplementary G), with a cubic or a star-like shape are circled. Those precipitates are located at the boundaries of the melt pools where the cooling rate is lower, compared to the melt pool center. Cooling time is thus sufficient at these boundaries for some precipitates to form while Zr stays in solid solution in the center of the melt pools [62,63]. Those primary precipitates act as nucleation sites for α-Al grains and are therefore known to promote a reduction in grain size leading to a bimodal structure with fine equiaxed grains at the melt pool boundaries and coarse grains in the center of melt pools (see Fig. 3). Indeed, this bimodal grain size distribution has already been observed and studied in other Al-Mg-Zr alloys [28,61–63]. Fig. 3b shows a random crystallographic orientation in the sample, while melt pool boundaries are highlighted by white lines. Fig. 3a shows the area density distribution of grains. The methodology used to compute this histogram is based on [64] and is explained in Supplementary H. It gives an area weighted average grain size of $1.4 \pm 0.8\,\mu m$.

STEM/EDX chemical maps were acquired in both the fine grain zone (FGZ) and the coarse grain zone (CGZ). The network observed in Fig. 2b is assumed to be located in the CGZ. The STEM-EDX map in this region (see Fig. 4a) reveals Mg enrichment within this network, which is located at grain boundaries. This hypothesis is consistent with results obtained for other Al-Mg-Zr alloys [63,65]. This Mg-rich network could be beneficial for healing since grain boundaries can act as pipelines for diffusion [66]. In contrast to AlMg8 [15,16], no eutectic network is observed in AB Almazium®. This disappearance is attributed to the addition of Zr, consistent with previous reports on as-cast Al–Mg alloys where the incorporation of Sc led to a similar loss of eutectic structures [67,68]. As a consequence, unlike AlMg8 [15,16], eutectic melting is not expected to occur at 450 °C. No bulk melting of the material is expected below 548 °C (see Supplementary D). However, due to microstructural inhomogeneities and the presence of a Mg-rich network, highly localised melting may still occur. Even if a small amount of liquid forms locally, it remains spatially limited and is not expected to play a significant role in the overall healing mechanism. Above the solidus temperature, melting at grain boundaries is expected to initiate, and the resulting uniformly distributed liquid phase could enhance the healing ability, similarly to AlMg8 [15,16]. Presence of Fe-rich and Si-rich precipitates at grain boundaries is highlighted in maps in Fig. 4a. Fe and Si are common impurities in Al alloys and those precipitates were already observed in different studies on Al-Mg-Zr alloys produced by PBF-LB/M [26,62,65]. A STEM/EDX map acquired in the FGZ (see Fig. 4b) showed Mg-rich precipitates located at grain boundaries and triple junctions. No Mg-rich network was observed in this region.

Fig. 2c and d show the evolution of the microstructure of Almazium® after HHT at 540 °C for 30 min. No melt pool structures nor Mg-rich network are evidenced anymore. In higher magnification view (see Fig. 2d), needle-shaped white precipitates are observed. Based on different studies [65,69], those precipitates were identified as equilibrium $D0_{23}$ Al_3Zr precipitates. Such precipitates were already reported in Addalloy® [65] and are known to be incoherent with the Al matrix [69]. Thus, they will not significantly participate to precipitate hardening. EBSD analyses were also performed on sample after HHT (see Fig. 3e and d). Fig. 3d shows the area density distribution of grains. The analysis gave an area weighted average size of $13.7 \pm 11.7\,\mu m$. Abnormal grain growth is observed after HHT. Abnormal grain growth was already reported in Scalmalloy® by Chen et al. after a heat treatment at 500 °C for 2 h [70]. In their study, abnormal grain growth mainly takes place in FGZ and is assumed to be due to the coarsening of $Al_3(Sc,Zr)$. Indeed, the Zener pinning exerted by the precipitates on grain boundaries is known to be inversely proportional to the radius of precipitates. Coarsening of $Al_3(Sc,Zr)$ thus favours abnormal grain growth. For Almazium®, based on the growth of Al_3Zr precipitates observed in Fig. 2c and d, one of the

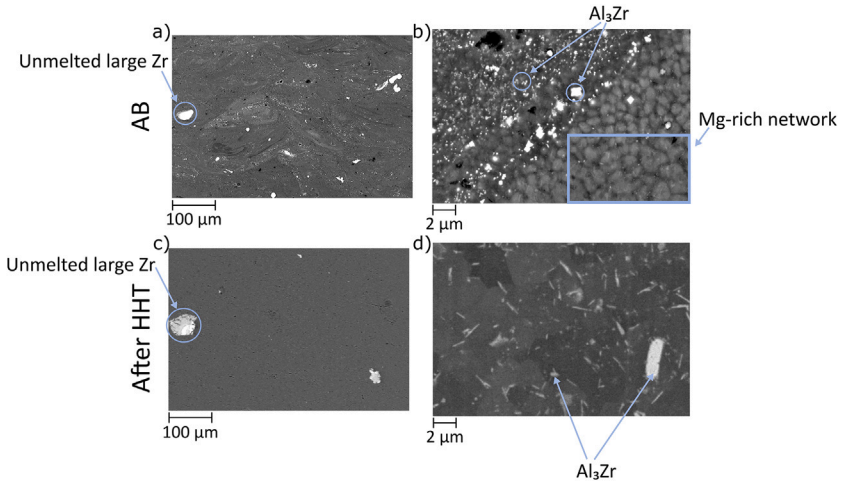

Fig. 2. Backscattered electron SEM micrographs showing the microstructure of Almazium® manufactured by PBF-LB/M: a) in AB state with unmelted Zr and b) Al_3Zr precipitates circled and the Mg-rich network inside the rectangle, c) after a HHT at 540 °C for 30 min and d) higher magnification view with white particles corresponding to Al_3Zr precipitates. (For interpretation of the references to colour in this figure legend, the reader is referred to the web version of this article.)

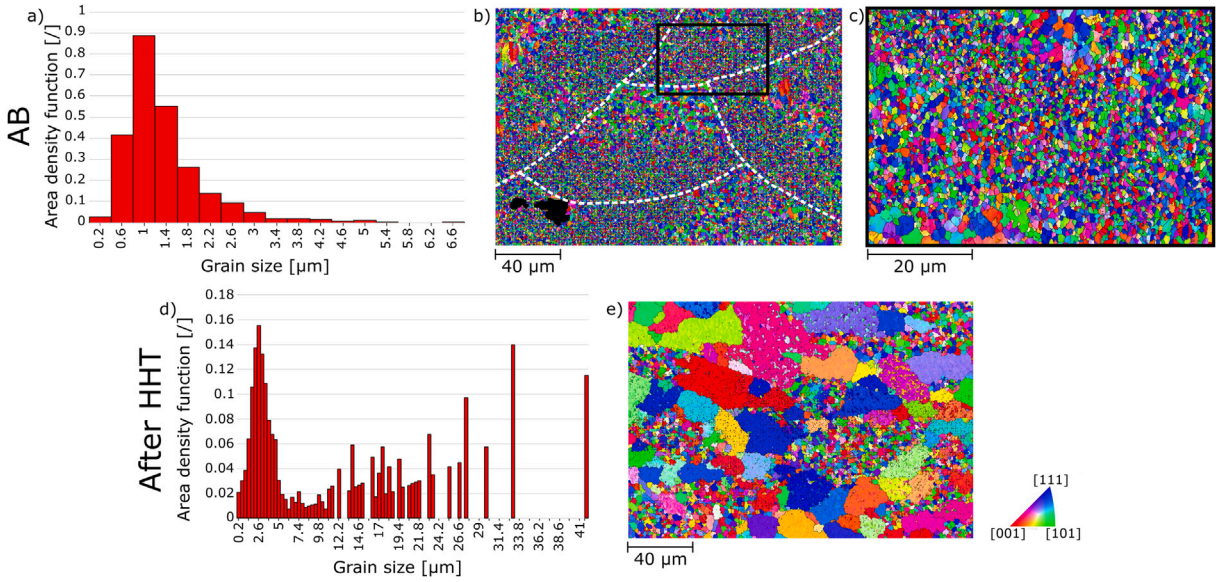

Fig. 3. a) Area density distribution of grains of AB Almazium® manufactured by PBF-LB/M, b) EBSD images showing the microstructure of AB Almazium® with black spots corresponding to unmelted Zr not taken into account and white lines representing melt pool boundaries, c) EBSD image of a zoom on the region squared in black in (b), d) the area density distribution of grains of Almazium® manufactured by PBF-LB/M after an HHT at 540 °C for 30 min and e) of Almazium® after HHT. (For interpretation of the references to colour in this figure legend, the reader is referred to the web version of this article.)

reasons explaining abnormal grain growth is assumed to be the decrease in Zener pinning.

To study the content of the solid solution, five AB samples were analysed with APT (see Fig. 5a for a representative sample). Table 2 shows the average and standard deviation (five samples for both AB and after HHT) of the chemical composition of the solid solution of the α-Al phase. Firstly, Mg content in solid solution is about 33 times what is expected based on Thermo-Calc computation at equilibrium for Almazium® composition at ambient temperature (around 0.26 wt%). High cooling rate of PBF-LB/M is known to increase the amount of atoms in solid solution leading to a supersaturated solid solution [71]. This higher Mg content is an advantage because it means that solid solution hardening will be more effective. In addition, there is more Mg available for diffusion during the healing treatment, expectedly improving the healing efficiency. From a diffusion perspective, the amount of material available to fill a void scales with the cubic root of the local Mg concentration in solid solution. Consequently, increasing Mg retention would directly increase the maximum healable void volume (see Supplementary I). The lower Mg content measured by ICP compared to APT (Tables 1 and 2) arises from the large difference in sampling volumes. APT probes an extremely localised region ($200 \times 100 \times 100\,nm^3$), whereas ICP averages over the bulk material (several mm^3). As a result, APT is sensitive to local Mg-enriched domains, while ICP captures both Mg-rich and Mg-poor regions (see Fig. 2a), yielding a lower average concentration. Conversely, the Zr content in solid solution appears lower by APT than by ICP, since ICP also accounts for primary precipitates, whereas APT measures only the solute fraction. Nevertheless, the Zr content in solid solution in Almazium® exceeds the equilibrium solubility according to Thermo-Calc ($5e^{-9}$ wt%). In total, six nanometric Mg-rich precipitates were also identified via APT in the five AB samples (see Fig. 5a) for a

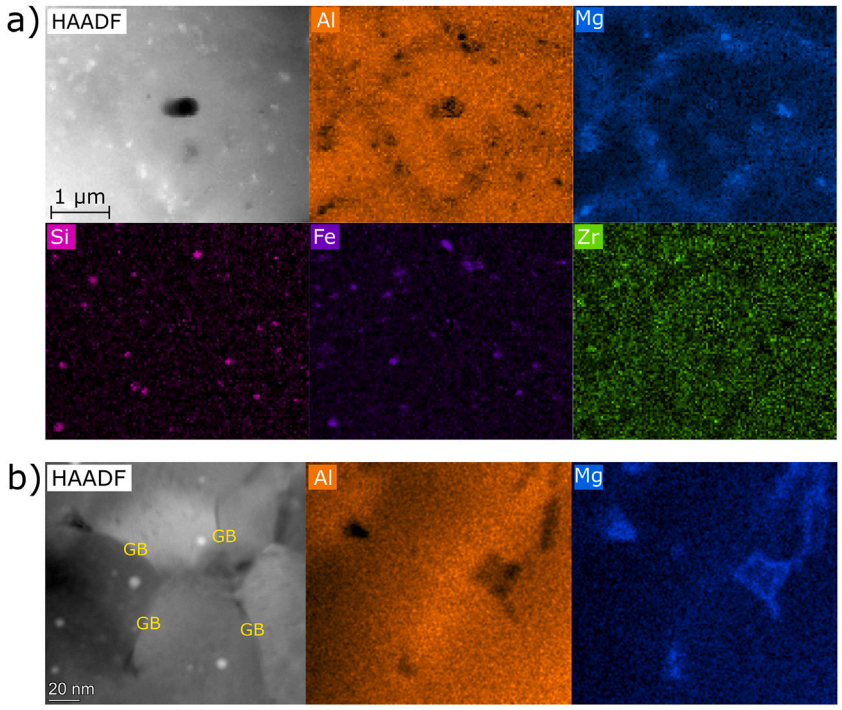

Fig. 4. STEM/EDX chemical maps a) in the CGZ with the Mg-rich network around an α-Al grain of an AB Almazium®, dark zone is assumed to be a void, and b) in the FGZ with Mg-rich precipitates at grain boundaries (GB).

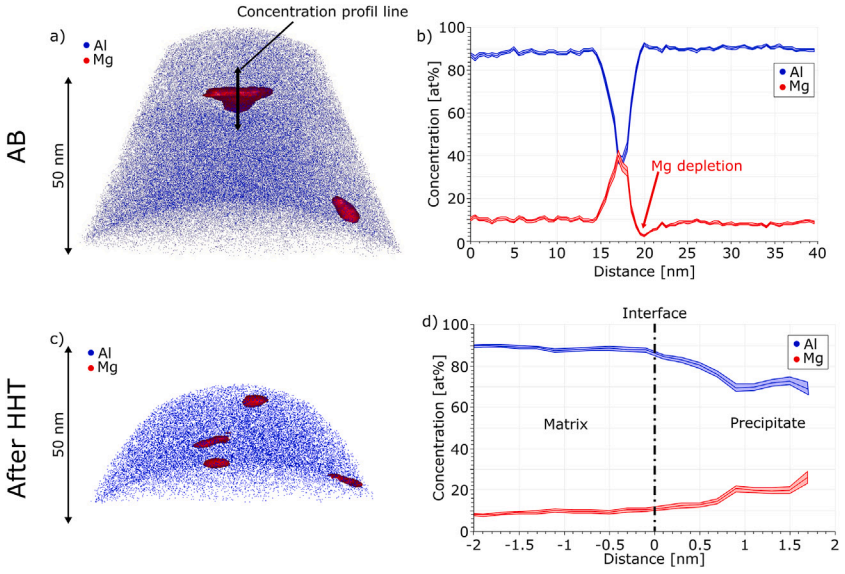

Fig. 5. APT volumes for Almazium® manufactured by PBF-LB/M with Al atoms in blue, Mg atoms in red: a) in AB state, c) after HHT at 540 °C for 30 min. b) the concentration profile across the grain boundary for a Mg-rich precipitate in AB sample represented by the double arrow in (a), and d) the proxigram at the interface between the matrix and a precipitate in sample in (c). (For interpretation of the references to colour in this figure legend, the reader is referred to the web version of this article.)

representative dataset). These precipitates are predominantly located at grain boundaries which act as heterogeneous nucleation sites [47]. The concentration profile across a representative grain boundary (see double arrow in Fig. 5a in Fig. 5b) reveals a pronounced Mg enrichment at the precipitate, followed by a depletion in the surrounding matrix. The Mg content in the precipitate is not constant, probably due to a dilution effect occurring during the reconstruction of the 3D volume containing nanoscale precipitates [72]. Indeed, the precipitates might create evaporation artefacts and trajectory aberrations, leading to a "dilution" of the precipitate in the Al matrix in the 3D reconstructed volume, i.e., reduced Mg content and increased Al content in the precipitate. More details can be found in [54]. The Mg content within the precipitate reaches almost 40 at% in some zones, indicating that they could correspond to β-Al_3Mg_2 or $\beta' - Al_3Mg_2$ phases. High-resolution TEM characterisation would be needed to accurately identified those precipitates but is out of the scope of this work.

APT experiments were performed on five samples subjected to a HHT at 540 °C for 30 min. The average solid-solution compositions and associated standard deviations are summarised in Table 2. Compared to the AB state, the Mg concentration in solution decreases significantly after HHT,

Table 2
Average composition and standard deviation of the α-Al phase without nanometric Mg-rich precipitates obtained by APT for five samples of Almazium® manufactured by PBF-LB/M and for five samples after a healing heat treatment (HHT) at 540 °C for 30 min.

		Al	Mg	Zr	Si	Cu
AB	*Mean [wt%]*	bal	8.41	0.40	0.01	0.02
	St. Dev. [wt%]	–	0.37	0.13	0.006	0.007
	Mean [at%]	bal	9.27	0.12	0.01	0.007
	St. Dev. [at%]	–	0.41	0.04	0.005	0.003
After HHT	*Mean [wt%]*	bal	7.23	0.17	0.00	0.008
	St. Dev. [wt%]	–	1.10	0.09	0.00	0.01
	Mean [at%]	bal	7.97	0.05	0.00	0.004
	St. Dev. [at%]	–	1.20	0.03	0.00	0.005

providing evidence of Mg-rich precipitation. A total of six nanoscale Mg-rich precipitates were directly observed by APT (see Fig. 5c for a representative case). Fig. 5d shows a proxigram from the interface between the matrix and a Mg-rich precipitate from Fig. 5c. The Mg composition of the precipitate ranges around 26 wt%. Although the exact stoichiometry cannot be unambiguously determined due to potential signal dilution from the surrounding Al matrix, these nanoscale features can also be identified as possible $\beta' - Al_3Mg_2$ or $\beta - Al_3Mg_2$. A detailed TEM investigation would be required to determine which phase they are, quantify their volume fraction, size distribution, and morphology before and after HHT, which falls beyond the present scope. The observation of such nanoscale Mg precipitation is particularly relevant in the context of healing mechanisms. Precipitation of solute atoms at nano-voids has been documented in Al alloys [37,38]. In Almazium®, Mg remains in a supersaturated solid solution and diffuses approximately six times faster than Al self-diffusion in the matrix [38]. Mg therefore reaches nanovoids first, and homogenisation can occur if sufficient time is allowed for Al to diffuse (around 2 h in the case of Al-Mg-Er alloys [38]). In parallel, the Zr content in solid solution decreases drastically after HHT, reflecting the pronounced precipitation of Al_3Zr, as confirmed by SEM micrographs in Fig. 2c and d.

3.2. Healing by HHT

3.2.1. Reference healing conditions

Diffusion being a thermally activated process, a HHT at 540 °C for 30 min was chosen as the reference condition. This temperature corresponds to the highest possible below the solidus, thus avoiding any bulk melting, as confirmed by DSC measurements on AB Almazium® and by Thermo-Calc simulations, which indicate a solidus around 548 °C (see Supplementary D). The selected treatment conditions also align with the recommendations of Gheysen et al. [16], facilitating direct comparison with their work while ensuring effective solute mobility. Fig. 6a shows the volume before and after HHT obtained by X-ray nano-CT for a damaged sample with voids in blue. Tracking of the voids provides the evolution of dV (see Eq. 1) as a function of the initial equivalent diameter of voids (Fig. 6b). It is well established that some measurement uncertainty can arise from the segmentation and the blurriness of voids. This uncertainty will depend on the void size and is larger for smaller voids [73]. σ_{dV_i}, the error on the measurement of dV for void i, was quantified by estimating the propagation of grey level threshold variations on the detected void volumes, following an approach based on repeated segmentations. Only voids with σ_{dV_i} smaller than 10 % were considered in the quantitative healing analysis to ensure statistical robustness. Full details of the uncertainty estimation are provided in Supplementary E.

65 % of the voids smaller than 1 μm were totally healed while the remaining 35 % were partially healed with an average dV of -45 ± 25 %. This dispersion highlights the scatter in healing efficiency among voids of similar size. Some voids with an equivalent diameter larger than 1 μm and up to 3.7 μm were also totally healed during this HHT. In this sample, no growth of voids were observed. One hypothesis to explain the different healing efficiency for voids of the same size is their position. Voids close to grain boundaries could have an improved healability because grain boundaries act as short-cuts for atomic diffusion during healing. It could also be attributed to the heterogeneity of local strain field and dislocation density within grains. Those regions with a high dislocation density are expected to enhance Mg pipe diffusion, thereby improving the healing ability. Compared to the results reported for AlMg8 by Gheysen et al. for a HHT also at 540 °C for 30 min, healing appears to be less effective in Almazium®, with reductions in the number of voids of 95 % and 58 %, for AlMg8 and Almazium® respectively, and decreases in total void volume of 42 % and 24 %, respectively [16]. This reduced healing efficiency can be attributed to the absence of a eutectic network in Almazium®, which exhibits a melting temperature of 450 °C, and to the HHT temperature being below the solidus, preventing bulk melting. Both factors prevent formation of an interconnected liquid phase, thereby limiting solute transport and the closure of voids. Indeed, Gheysen et al. [16] estimated that the liquid healing agent in AlMg8 is able to flow along more than 260 μm in 30 min of HHT between 500 °C and 580 °C while Mg atoms will diffuse only of 21 μm during a HHT at 540 °C for 30 min in Almazium® (see Fig. I.1 in Supplementary I).

Some voids seem not to follow the general trend in Fig. 6b. These are discussed in Supplementary J.

Correlative tomography (see Fig. 1) has been made to ensure that voids were totally healed during the HHT at 540 °C for 30 min and that they are not just smaller than the detection limit (voxel size = 35 nm). A specific ROI in the nano-CT volume before HHT was selected (see Fig. 7). For the nano-CT results, contrast was enhanced and visualisation facilitated by generating a pseudo-2D image: for each set of 199 slices, the minimum and maximum grey level values were extracted, projected onto a single slice, and then combined to produce a Min/Max projection. The same methodology was applied to the PFIB-SEM volume, except that only the minimum grey level values were retained to generate Min projection of 139 slices. Element marked with circle was used as reference point to ensure that the same zones were examined, and voids healed during the HHT are indicated by the red arrows. After using PFIB to reach this zone in the healed sample, the PFIB-SEM images (Fig. 7c) confirmed that no remaining voids were visible. It is important to pay attention to the voxel size of both techniques. In the case of nano-CT, the voxel size was $35 \times 35 \times 35\,nm^3$ while it was $25 \times 25 \times 50\,nm^3$ for PFIB-SEM. This means that PFIB-SEM images have a better X-Y resolution than X-ray nano-CT while Z resolution is better in the case of X-ray nano-CT. However, in Fig. 7, some voids are visible in PFIB-SEM projection but not in nano-CT before or after HHT (see green arrow for a representative example). These voids are smaller than the nano-CT detection limit (approximately 0.1 μm). No voids were observed in nano-CT after HHT but not in PFIB-SEM projection. Thus, despite the small Z pixel size of nano-CT, it is assumed that the absence of voids after HHT in nano-CT and PFIB-SEM projections (see Fig. 7b and c) suggests that those voids were fully healed. Some features do not look exactly the same in each image of Fig. 7 because the sample has been slightly tilted when switching from nano-CT to PFIB-SEM.

The observed healing mechanism is consistent with the hypothesis developed by Arseenko et al., which has not yet been proven [37]. Because of the high cooling rate inherent to PBF-LB/M, vacancies are trapped and dislocations are created in the matrix [74]. Mg atoms tend to be coupled with those vacancies and dislocations [75,76]. During HHT, grain boundaries act as sinks for vacancies and dislocations travelling from the matrix towards grain boundaries [37]. Mg atoms follow those voids and diffuse rapidly in grain boundaries to reach voids to reduce their interfacial energy, similar to sintering phenomenon [77]. Mg diffuses around six times faster than Al [38], but if the HHT is sufficiently long, Al will follow the same path to homogenise the microstructure. Although direct evidence at healed void surfaces is not available in the present study, the combined observations of solute redistribution by APT

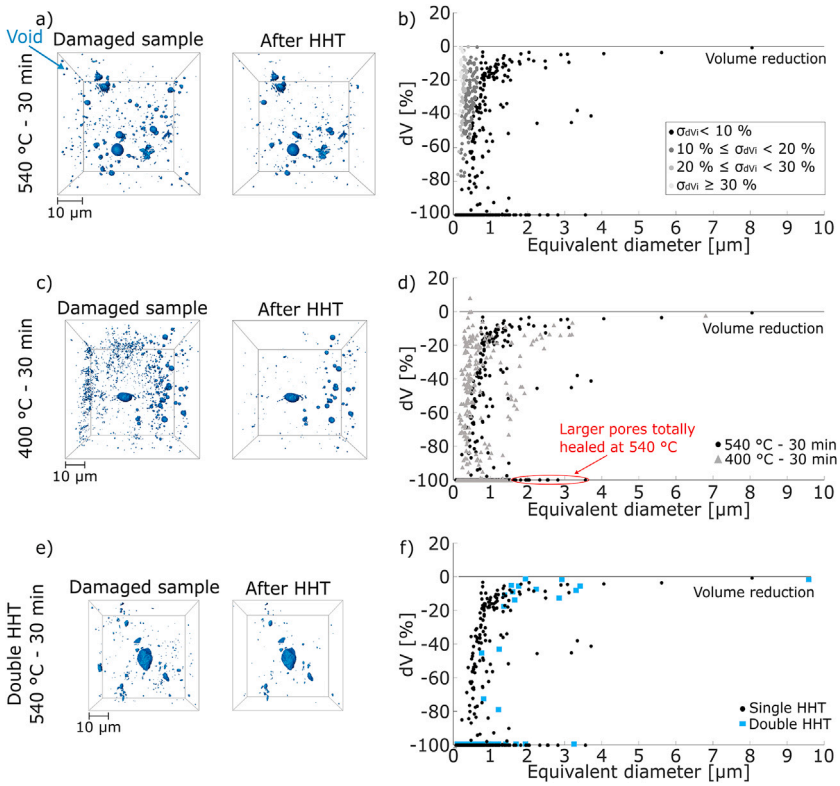

Fig. 6. X-ray nano-CT volumes of damaged Almazium® alloy a) before and after healing heat treatment (HHT) at 540 °C for 30 min, c) before and after healing heat treatment at 400 °C for 30 min, and e) a healed then damaged Almazium® sample before and after healing heat treatment at 540 °C for 30 min. Voids are in blue. The evolution of dV as a function of the initial equivalent diameter of voids b) after HHT at 540 °C for 30 min with grey levels showing σ_{dV}, the error on dV for each void, d) comparison after HHT at 540 °C for 30 min and after HHT at 400 °C for 30 min represented by black points and grey triangles respectively, and f) comparison after single HHT at 540 °C for 30 min and after second HHT cycles at 540 °C for 30 min represented by black points and blue squares respectively. (For interpretation of the references to colour in this figure legend, the reader is referred to the web version of this article.)

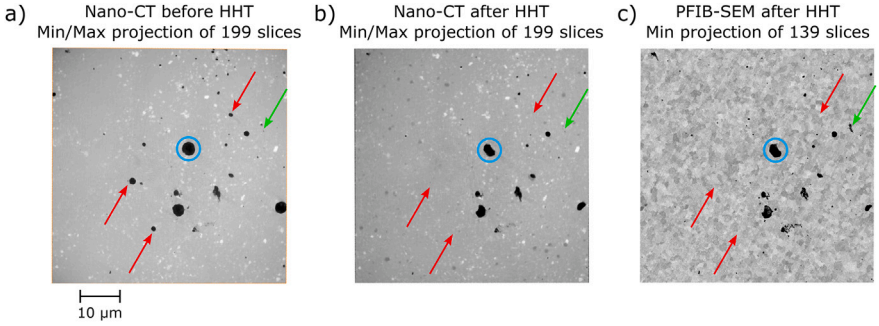

Fig. 7. Nano-CT Min/Max projections of 199 slices of the same ROI in a damaged Almazium® sample: a) before and b) after a HHT at 540 °C for 30 min and c) PFIB-SEM Min projection of 139 slices of the same ROI after HHT. The reference point used to relocate the same zones is circled in blue. Red arrows indicate voids healed during HHT, while green arrows highlight a void visible in the PFIB-SEM projection but below the detection limit in the nano-CT projections before and after HHT. (For interpretation of the references to colour in this figure legend, the reader is referred to the web version of this article.)

(see Table 2) and the size dependent void closure revealed by X-ray nano-CT (see Fig. 6b) provide indirect support for this interpretation. Overall, the results point to diffusion-driven healing as the dominant mechanism under HHT conditions, while acknowledging that future site specific analyses are required to fully exclude any contribution from highly localised liquid-assisted phenomena.

3.2.2. Comparison with lower temperature and HHT time

The same methodology as for the sample shown in Fig. 6a, b was applied to a damaged Almazium® sample, but using a HHT at 400 °C for 30 min at ID16b (ESRF) (see Fig. 6c, d). At the end of the HHT, cooling was performed rapidly by removing the furnace. The treatment time was kept at 30 min to compare with Fig. 6a and b. The choice of 400 °C was guided by diffusion considerations. The longest diffusion path for Mg to heal a void was assumed to extend from a grain boundary to the grain center, since a Mg-rich network was observed along grain boundaries (Fig. 4). Using the largest grain of the AB sample obtained in Fig. 3, this maximum distance was estimated to be 3.29 µm. Calculations of diffusion healing times for this distance as a function of temperature indicated that 400 °C is an appropriate candidate, as Mg can reach the grain center in less than 25 min (see Supplementary I). Moreover, selecting this temperature ensures a significant ΔT relative to 540 °C, thereby

highlighting the effect of temperature on the healing kinetics since the healing time is estimated at 42 s at 540 °C to reach the center of the largest grains.

Fig. 6c shows the volume before and after HHT obtained by X-ray nano-CT with voids in blue. Similarly to Fig. 6a, the smallest voids were healed during the HHT. Tracking of the voids provided a comparison of the evolution of dV as a function of the initial equivalent diameter of voids (Fig. 6d) after HHT at 540 °C for 30 min and HHT at 400 °C for 30 min represented by black points and grey triangles respectively. Only voids with a σ_{dV_i} smaller than 10 % are represented in Fig. 6d. 90 % of the voids smaller than 1 μm were totally healed. Growth of one void was observed. This void has an equivalent diameter of 0.44 μm and its growth is about 8 %. The healing at 400 °C allows healing for voids up to 1.5 μm while healing at 540 °C showed total healing for voids up to 3.7 μm. However, 400 °C is more effective to completely heal voids smaller than 1 μm, i.e., 90 % completely healed at 400 °C versus 65 % at 540 °C. A comparison of the initial void size distributions indicates that the samples treated at 400 °C and 540 °C do not exhibit identical void populations (see Supplementary K). The sample treated at 400 °C contained 1559 voids smaller than 1 μm, whereas the sample treated at 540 °C contained 255 voids in the same size range. The probability density reported in Supplementary K further confirms that the 400 °C sample contains a higher fraction of voids below 0.7 μm. Since smaller voids are more readily healed, this difference in initial void populations may partly explain why the HHT at 400 °C appears more effective for voids smaller than 1 μm compared with the HHT at 540 °C. Another possible explanation is the increase in gas pressure within gas-filled voids at higher temperatures [77], which could hinder void closure at 540 °C compared with 400 °C. However, this interpretation is inconsistent with the larger voids healed at 540 °C (see Fig. 6d), which would need to be gas-free. The only expected gas-free voids are damage-induced voids, which are estimated to be submicrometric (see Section 3.2.3), far smaller than the 3.7 μm maximum healed void. Therefore, gas pressure is unlikely to be the dominant factor, and differences in the initial void size distributions are more likely responsible for the observed healing behaviours.

The impact of the time of the HHT was also studied for a single healing at 540 °C and for single healing at 400 °C. Fig. 8 shows the evolution of the densification [%] as a function of the HHT time for the two healing temperatures. Densification is defined as

$$\text{densification} = \frac{\text{density}_{\text{after}} - \text{density}_{\text{before}}}{\text{density}_{\text{before}}} * 100 \quad (2)$$

Bars in Fig. 8 represent the uncertainty in the measurement of the densification and the methodology used to compute it is explained in Supplementary E. In the case of the HHT at 400 °C, uncertainty bars are too small to be easily distinguished. In both cases, densification is initially rapid but slows down after approximately 10min. The time of the HHT could thus be reduced to 10 min without impairing the healing efficiency. This is consistent with the observations of Arseenko et al., who reported that a holding time of 10 min is already sufficient in a 6063 Al alloy to significantly reduce the void volume fraction during HHT at 400 °C [37]. The densification is faster in the case of the healing at 540 °C than at 400 °C and the final densification reached is double. This result matches the expected behaviour, i.e., healing at higher temperature is faster than at lower temperature. Moreover, because Mg diffuses more slowly at 400 °C, a larger fraction of it may be consumed by the formation of second-phase particles, thereby reducing the amount of Mg available to contribute to healing. However, it is important to note that the two samples did not start with the same density. The sample used at 540 °C had a relative density of 98.92 % at time 0 while the sample used at 400 °C had a relative density of 99.77 %. It could be more difficult to further increase the density with an initially dense sample, explaining why the densification by diffusion is slower here.

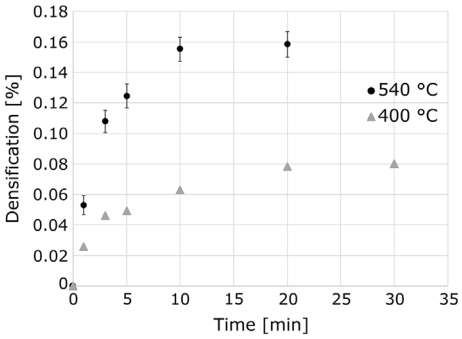

Fig. 8. Comparison of the evolution of the densification [%] (see Eq. 2) as a function of the time of the HHT for single healing at 540 °C (points) and at 400 °C (triangles) for 30 min in both cases. Bars represent the uncertainty in the measurement of the densification.

3.2.3. Possibility to perform two healing cycles

Having established that a first healing is possible, the question of second healing cycle will now be addressed. A tensile sample underwent a HHT at 540 °C for 30 min prior to the tensile test. The goal was to heal the voids due to PBF-LB/M manufacturing a first time. As already shown in Fig. 6b, preferential healing of manufacturing voids smaller than 1 μm is expected. Then, tensile testing induced damage inside the sample which was subsequently prepared for X-ray nano-CT (see Section 2.4). Inspection of the fracture surfaces revealed the presence of small and large fractured Al_3Zr precipitates, suggesting that they can act as nucleation sites for damage (see Supplementary L). Assuming that most of the voids smaller than 1 μm were healed during the first HHT, new submicron voids observed are likely associated with the fracture of small Al_3Zr precipitates. This interpretation is consistent with the measured equivalent diameter of those precipitates of 0.48 μm.

During the beamtime at ESRF, the sample was initially scanned before the application of a second HHT at 540 °C for 30 min, after which it was scanned again. Fig. 6e shows the volumes obtained by X-ray nano-CT. The smallest voids are healed during the second HHT. The comparison of the evolution of dV as a function of the initial equivalent diameter of voids is provided (see Fig. 6f) after one HHT at 540 °C for 30 min and two HHTs at 540 °C for 30 min represented by black points and blue squares respectively. Only voids with a σ_{dV_i} smaller than 10 % are represented. Note that two times less voids were found in that sample (291 voids) compared to the previous sample (see Section 3.2.1) with 517 voids before healing. It is thus assumed that the number of voids was already reduced during the first HHT prior to the tensile test. In the case of double healing, 99 % of the voids smaller than 1 μm are completely healed during the second HHT, and few voids up to 2 μm are also totally healed. These results indicate that the healing mechanism remains active after a first healing cycle and subsequent damage, demonstrating the repeatability of the healing process. Several hypotheses may account for the improved healing efficiency of voids < 1 μm after two healing cycles, compared with the 65 % fully healed after a single 30 min HHT at 540 °C. First, some voids inherited from PBF-LB/M can contain trapped gas [29], whereas damage-induced voids generated during tensile loading are essentially vacuum-filled, making them easier to close. Second, voids present before the first HHT experience a second annealing step, providing an additional 30 min for gas to diffuse out of the void and for Mg to diffuse in, thereby enhancing the healing efficiency. The possibility of multiple healing has already been demonstrated for a Ti alloy coated with a low–melting point healing agent [78], and is considered, in principle, infinitely repeatable in the case of shape-memory alloys [79]. However, to the authors' knowledge, this is the first experimental evidence of multiple healing predominantly driven by diffusion-based mechanisms. Analysis of Fig. 2, shows that, as predicted at equilibrium, the Mg-rich network dissolves during heat treatment, yielding a

stable, fully α-Al microstructure. Even if no Mg-rich network remains for healing after the first HHT, APT results (Table 2) showed that Mg is still available in supersaturated solid solution and temperature of the HHT is high enough to trigger diffusion.

3.3. Healing by healing heat and pressure treatment (HHPT)

To study the healing by HHPT, a sample manufactured with the optimal parameters was prepared as described in Section 2.4 and scanned after LBPF at ESRF before applying the HIP treatment at 540 °C for 30 min and at 300 MPa at Université Sorbonne Paris Nord. The sample was sent back to ESRF and scanned again after the HHPT. Fig. 9a shows the X-ray nano-CT slices of the same volume before and after the HHPT. A particle used as a reference point is circled in red. The voids disappearing during the treatment are circled in blue. The white zone on the left is a Zr particle. When looking at the voids in the overall volume of the sample (see Fig. 9b), no voids were visible after HHPT. In this sample, the biggest void observed and healed was about 4.7 µm in equivalent diameter.

To assess the efficiency of the HHPT, a second sample was studied. It consists of a piece of a cube manufactured with poor printing parameters (a laser power of 218 W, a scanning speed of 200 mm/s and a hatch spacing of 100 µm) leading to a very low relative density, i.e., around 94 %. This sample was scanned before and after the HHPT with a laboratory tomograph from RX Solutions and a voxel size of 5 µm. Fig. 9c shows the same slice of the sample before and after HHPT. Fig. 9d shows the 3D volume of voids inside this sample before and after HHPT, with the contour of the sample in grey. All the voids in the sample with an equivalent initial diameter up to at least 100 µm, were healed or became smaller than the detection limit of tomography during the HHPT. A rule of thumb for tomography is that features smaller than 3 times the voxel size cannot be distinguished from the noise, meaning in this case that if voids are not totally closed but are smaller than 15 µm, they will not be identified. The only remaining voids are the open voids, i.e., those located on the edge of the sample. During the HHPT, the gas from the HIP chamber enters those open voids, preventing their healing [80].

The improved healing efficiency of HHPT is attributed to the combined effect of plastic deformation, creep behaviour and healing consistent with diffusion-driven mechanism [1]. Simulations of AlSi10Mg during HIP at different temperatures and holding times showed that porosity reduction was mainly achieved through plastic deformation, facilitated by the reduction in the material's yield strength with increasing temperature [30]. It is assumed that once the voids reach a critical dimension, previously shown to be below approximately 2 µm (see Fig. 6), diffusion-driven mechanisms become effective and ensure their sealing. Gheysen et al. [16] proposed several hypotheses to explain the origin of the material filling the voids: (i) relocation of voids to less detrimental sites, (ii) overall volume shrinkage, and (iii) local volume expansion associated with phase transformations and/or relaxation of residual stresses. Total volume measurements indicate that the sample underwent a 10 % shrinkage during HHPT. This value corresponds to a reduction of $\sim 9.3\,mm^3$ of the total sample volume and was measured over a region of interest including the entire specimen. For the poorly printed sample, the initial relative density of 94 % corresponds to a void volume of $\sim 6.5\,mm^3$. This correspondence indicates that, in this case, the material filling the voids primarily originates from shrinkage of the part.

The alloy was initially designed to promote healing of service-induced damage. The present results further demonstrate that the HHT and HHPT treatments can also reduce manufacturing-induced porosity. It should be noted, however, that the process primarily targets void-type defects and is not intended to fully recover plastic deformation. This effective healing by HHPT thus opens the possibility of manufacturing parts without fully optimised process parameters, while still achieving a dense final component after HHPT. Considering that PBF-LB/M parameters are often optimised using cubic samples and are difficult to generalise to all geometries [81], developing healable alloys is of particular interest to relax process constraints while still achieving fully dense parts. This could also be attractive for industrial applications, where faster processing conditions may be used to reduce production time while ensuring full densification after HHPT. However, the shrinkage occurring during HHPT must be accounted for in process modelling.

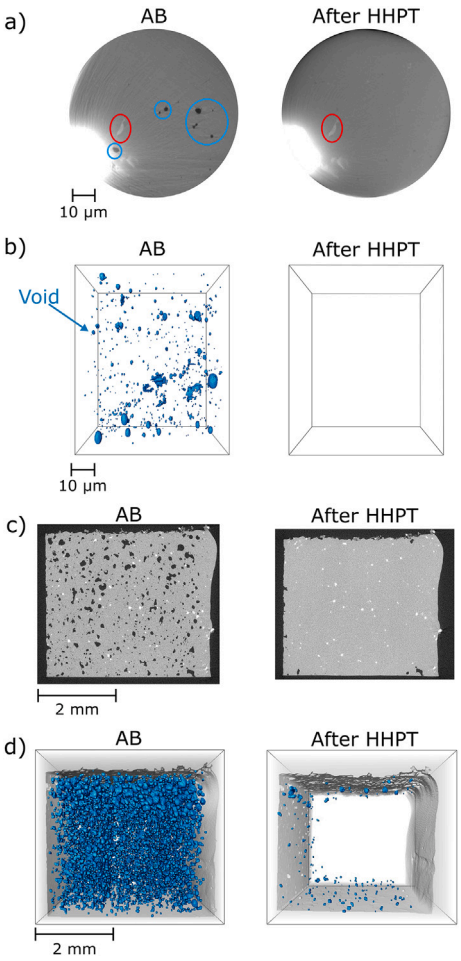

Fig. 9. a) X-ray nano-CT slices of a sample of Almazium® manufactured by PBF-LB/M before and after a HHPT applied with a HIP. In red, a particle being a point of reference and in blue, voids healed during the HHPT. The bright white region corresponds to an unmelted Zr particle. b) 3D representation of voids (in blue) inside the sample in (a) before and after the HHPT. c) Laboratory tomography slices of a sample of Almazium® manufactured by PBF-LB/M before and after a HHPT applied with a HIP. d) 3D representation of voids (in blue) inside the sample in (c) before and after the HHPT with the contour of the sample (in grey). (For interpretation of the references to colour in this figure legend, the reader is referred to the web version of this article.)

3.4. Static mechanical properties

As shown in Section 3.2, healing is observed for various time of HHT (between 1 and 30 min) and also for different temperatures (400 and 540 °C). It is well established that heat treatment can affect the mechanical properties of an alloy through different mechanisms. Fig. 10a shows the impact of the temperature for an isochronal treatment of 30 min on the mechanical properties of Almazium® (one sample per condition). Fig. 10b shows the impact of the duration of an isothermal treatment at 540 °C (one sample per condition). In both figures, the grey curve represents the engineering tensile curve for the AB AlMg8 [15]. Table M.1 (see Supplementary M) presents the values of the yield strength σ_y, the ultimate tensile strength σ_{UTS} and the engineering elongation at fracture

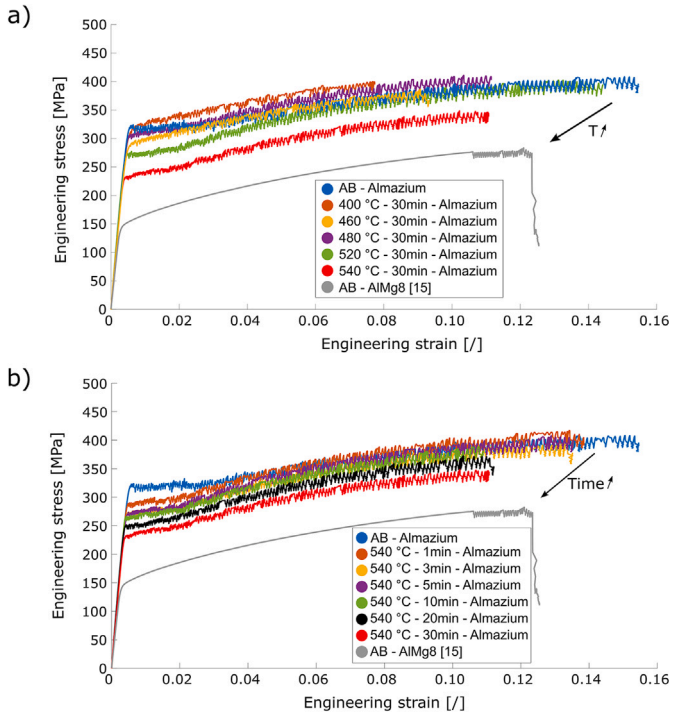

Fig. 10. Engineering stress ([MPa]) as function of the engineering strain ([/]) for tensile tests made on Almazium® samples after HHT at a) 30 min and for different temperatures, and b) 540 °C and for different times. In both figures, Almazium® results are compared to the tensile curve of the AB AlMg8 [15] (grey curve), i.e., without Zr.

$\epsilon_{f,eng}$ for each tested sample. The yield strength of AB Almazium® is 317 MPa compared to 132 MPa for the AB AlMg8 [15], i.e., the yield strength was doubled following the addition of Zr. Ductility measured by the fracture strain, around 15 %, is more or less identical in Almazium® and in AlMg8. As a comparison, Scalmalloy®, a high-strength Al-Mg alloy, has a yield strength of 470 MPa and a ductility of 13 %[82]. In addition, σ_y, σ_{UTS} and $\epsilon_{f,eng}$ tend to decrease compared to AB Almazium® for longer time during isothermal tests. In the case of the isochronal tests, a first decrease in σ_{UTS} and $\epsilon_{f,eng}$ is observed for the treatment at 400 °C. They then start to increase for treatments between 460 °C and 520 °C before decreasing for the treatment at 540 °C. Concerning the σ_y, a decreasing tendency is observed when the temperature of the treatment is increased.

Since only one specimen per condition was tested due to limited material availability, the mechanical results should be interpreted in terms of consistent trends rather than statistically averaged values, especially considering the intrinsic scatter typically observed in PBF-LB/M materials [83]. Furthermore, the initial porosity of the tensile specimens was not measured prior to mechanical testing. Although all samples were produced using identical PBF-LB/M parameters, variations in porosity reduction induced by the different healing heat treatments may have influenced the mechanical response. Consequently, the effect of porosity reduction cannot be fully separated from concurrent grain coarsening and precipitate evolution, and the mechanical results are therefore discussed primarily on a qualitative and comparative basis.

3.4.1. AlMg8 vs Almazium®

To understand the increased mechanical properties of AB Almazium® compared to AB AlMg8, the yield strength mechanisms was studied. The yield strength (σ_y) is decomposed as the sum of different contributions following conventional strengthening models for Al based alloys (Eq. 3) [63,84]. Grain boundary strengthening (σ_{GB}) is estimated using a Hall–Petch equation adapted to the bimodal grain size distribution. Solid solution strengthening (σ_{SS}) is evaluated based on measured solute contents. Particle (σ_P) and dislocation wall strengthening (σ_{DW}) are qualitatively assessed. The details of the computation of contributions to σ_y are given in Supplementary M.

$$\sigma_y = \sigma_{GB} + \sigma_{SS} + \sigma_P + \sigma_{DW} \tag{3}$$

- For AlMg8, the grain size d was measured at 6.6 µm [15], leading to a σ_{GB} of about 86 MPa (see Eq. M.1 in Supplementary M). As already explained in Section 3.1, Almazium® has a bimodal microstructure, with a fine grain zone (FGZ) and a coarse grain zone (CGZ). The threshold diameter between FGZ and CGZ was set at 2 µm [85]. Eq. M.1 can thus be adapted to take into account the grain size for the two zones (d_{FGZ} and d_{CGZ}) and the fraction of FGZ and CGZ (f_{FGZ} and f_{CGZ}) (Eq. 4).

$$\sigma_{GB} = \sigma_0 + k\left(\frac{f_{FGZ}}{\sqrt{d_{FGZ}}} + \frac{f_{CGZ}}{\sqrt{d_{CGZ}}}\right) \tag{4}$$

  EBSD analysis from Section 3.1 allows the estimation of $d_{AB,FGZ}$, $d_{AB,CGZ}$, $f_{AB,FGZ}$ and $f_{AB,CGZ}$ for AB sample (see Table M.2 in Supplementary M). σ_{GB} was estimated at 173 MPa for Almazium®. Zr addition allows thus to double the σ_{GB}.
- In the case of AlMg8, the only element in solid solution is Mg and its atomic concentration $c_{AlMg8,Mg}$ was estimated at 9.2 %at [58], giving a solid solution strengthening (σ_{SS}) of 100 MPa (see Eq. M.2). For Almazium®, both Mg and Zr are present in solid solution. The atomic concentration used ($c_{AB,Mg}$ and $c_{AB,Zr}$) are the ones obtained with APT and presented in Table M.2 (see Supplementary M), giving a total σ_{SS} of 106 MPa. The Zr content in solid solution is low, resulting in an insignificant contribution to σ_{SS} (~5 MPa).
- It is first assumed that precipitation in AlMg8 and in AB Almazium® will be similar, leading to σ_P of same levels. The only difference is Zr addition in the case of Almazium®. Usually, only primary Al_3Zr are observed in the border of melt pools (see Section 3.1). Those precipitates are quite large and their size is estimated between 100 and 400 nm [62]. The volumetric fraction ϕ of the Al_3Zr precipitates in Almazium® is not known. However, data available in literature indicate a ϕ smaller than 1 % for AB Al-Mg-Zr alloys [26,63]. Even if the extreme case of $\phi = 1\,\%$ is assumed, the σ_P of Al_3Zr precipitates will be only about 28 MPa for precipitates with a diameter of 100 nm and this value decreases when the diameter is increased. It means that Al_3Zr precipitates are not the main contribution to the yield strength in AB Almazium®.
- The dislocation density was not measured for AlMg8 nor in this study. However, since PBF-LB/M have been used to manufacture AlMg8 and Almazium®, it is assumed that dislocation density is of the same order of magnitude. σ_{DW} is thus similar for both alloys.

The final σ_y is about 186 MPa for AlMg8 and about 279 MPa for Almazium®. The apparent overestimation of σ_y in AlMg8 arises from relying on EDS to quantify Mg in solid solution. Some eutectic network rich in Mg could be present just below the surface and could have been taken into account since the spatial resolution of EDS is around 1 μm^3 [86]. It is also worth noticing that the σ_P and σ_{DW} were not considered in this case but should also increase σ_y, explaining the underestimation for Almazium®. Based on the available experimental evidence, grain refinement is the only mechanism whose magnitude is sufficiently large to account for the observed strength increase in σ_y for Almazium® compared to AlMg8. The other mechanisms (solid solution, particles, dislocations) likely contribute but cannot, within reasonable bounds, reproduce the measured yield strength without invoking grain refinement as a major factor.

Regarding the ductility, it is surprising to have a similar $\epsilon_{f,eng}$ between AlMg8 and Almazium®. Indeed, it is usually assumed that

strength improvement leads to a decrease in ductility [87]. The impressive stability of $\epsilon_{f,eng}$ with Zr addition, despite the enhancement of σ_y, is attributed to the bimodal microstructure. CGZ can resist higher deformation than FGZ during tensile tests [63]. CGZ will first begin to deform plastically while FGZ continues to deform elastically, creating a partitioning of the strain. Several studies have shown that a bimodal structure allows to improve $\epsilon_{f,eng}$ by inducing strain hardening mechanisms that stabilise tensile deformation [28,88].

A Portevin-Le Chatelier (PLC) effect is observed for all samples in Fig. 10. It is commonly assumed that this effect is the result of dynamic strain ageing (DSA) in which the mobile dislocations will interact with solute atoms during plastic deformation [89]. During deformation, dislocations are pinned by solute atoms acting as obstacles leading to an increase in the stress. Once the applied stress becomes sufficiently high, specific dislocation sources can be activated and release a large number of mobile dislocations (so-called dislocation bursts), causing a stress drop [90]. This process creates serrations observable in the stress-strain curve. For Almazium®, serrations are identified as type B for small strain before changing into type C until fracture. Types B are characterised by serrations about the general stress-strain curve while types C are characterised by a stress drop below the general level of the stress-strain curve [89,91]. For AlMg8, serrations are type C. In this case, strain localisation bands appear randomly within the material and remain static [92]. In contrast, type B serrations involve the so-called "hopping bands," where a deformation band forms and then disappears as a new band nucleates just ahead of it, giving the impression of a forward, stepwise propagation [91]. In both materials, the presence of type C serrations indicates a risk of strain localisation. It is also well established that PLC effect will start at a critical deformation called ϵ_c which can vary depending on different parameters such as the Mg content in solution or the grain size [93,94]. In particular, ϵ_c has been shown to increase with grain size [93]. Since AlMg8 has a larger grain size than Almazium®, this could explain why the serrations appeared at different deformations.

3.4.2. Impact of time and temperature of the HHT

To understand the mechanical behaviour of Almazium® depending on the temperature and the time of the HHT, the different contributions to σ_y (Eq. 3) are studied again.

- As shown in Eq. 4, σ_{GB} depends on the average grain size in FGZ and CGZ and on their area fraction. EBSD analysis made on Almazium® samples after HHT at 400 °C, 480 °C and 540 °C for 30 min allowed to study the evolution of those different parameters (see Table M.2 in Supplementary M). f_{FGZ} decreases (f_{CGZ} increases respectively) as the temperature of HHT increases. The higher the temperature, the larger the contribution of coarse grains to σ_{GB}. However, large grains are not effective for hardening and d_{CGZ} also tends to increase between 400 °C and 540 °C, reducing further the σ_{GB}. In the end, σ_{GB} of 155 MPa, 129 MPa and 75 MPa are obtained for Almazium® samples after HHT at 400 °C, 480 °C and 540 °C for 30 min respectively. It is assumed that the behaviour will be identical for isothermal conditions, the longer the HHT, the larger the grains in CGZ and its area fraction, leading to a smaller σ_{GB}.
- Another aspect to take into account is the impact of the solid solution on σ_{SS}. First, Zr in solid solution will precipitate to form Al_3Zr, meaning that the contribution of Zr to σ_{SS} will be reduced compared to the AB Almazium®. Table 2 shows that Zr content in solid solution drops from 0.12 at% to 0.05 at%. However, it was already determined earlier that this contribution does not have a significant impact on σ_{SS} and can thus be neglected (only 3 MPa). To continue, the amount of Mg in solid solution was reduced after the HHT at 540 °C for 30 min from 9.27 at% to 7.97 at% (see Table 2), leading thus to a decrease in σ_{SS}. This decrease is however estimated to only 10 MPa. It is thus assumed that the change in σ_{SS} will not be the main contribution to explain the different mechanical behaviours for both isochronal and isothermal conditions.
- APT results (see Fig. 5) show presence of Mg-rich nano-precipitates in AB Almazium® and also after HHT at 540 °C for 30 min. It is assumed that those precipitates have a similar size and that they will participate in the same way to σ_P. The focus will be placed on Al_3Zr precipitates in the following.

  The different contributions to σ_P depend on the size and volume fraction of the precipitates (see Supplementary M). Fig. M.1 in Supplementary M illustrates the influence of precipitate radius and volume fraction ϕ on σ_P, showing that an optimal size exists for Al_3Zr to maximize hardening and that higher precipitate volume fractions lead to increased σ_P. In AB Almazium®, the only Al_3Zr present are primary precipitates, which are too large to contribute to strengthening. Heat treatment enables Zr in solid solution to precipitate, with the resulting size and volume fraction of precipitates controlled by the temperature and duration of the treatment. These precipitates effectively harden the alloy as long as they adopt the $L1_2$ structure and remain coherent with the matrix. Above 460 °C, Zr precipitates transition to non-coherent, stable $D0_{23}$ structures, resulting in a decrease in σ_P [63]. Consistently with our observations, Knipling reported a significant reduction in the hardness of Al–Zr alloys when either the duration of a 500 °C heat treatment was increased or a 3 h treatment exceeded 500 °C [60]. This behaviour was attributed to the dissolution of nanometric $L1_2$ Al_3Zr followed by heterogeneous precipitation of $D0_{23}$ Al_3Zr. Knipling also demonstrated that increasing the temperature and duration of heat treatment leads to larger Al_3Zr precipitates with reduced volume fraction.
- During HHT, alloys are expected to undergo recovery phenomenon, leading to a reduction of dislocation density and thus a reduction of σ_{DW}.

In summary, the slight increase in σ_y, with values close to AB, observed for HHT at 400 °C, 460 °C, and 480 °C for 30 min (Fig. 10a) is attributed to sufficient Zr in solid solution precipitating as nano $L1_2$ Al_3Zr, which compensates for the loss of σ_{GB} due to grain growth. In contrast, the significant drop in σ_y at temperatures above 500 °C during isochronal testing, and the decrease in σ_y with time (Fig. 10b), is primarily due to grain growth reducing σ_{GB}. Precipitation cannot counterbalance this loss: although some nano $L1_2$ Al_3Zr may still be present, the dominant effect is the growth of non-coherent $D0_{23}$ precipitates (see Fig. 2d) and the reduction of their volume fraction, leading to a diminished contribution to σ_P.

In their work on Al-Si-Mg alloys, Hannard et al. reported that ductility increases with smaller particle size, periodic particle arrangements, and lower initial porosity [95]. As shown in Fig. 2d, coarse Al_3Zr precipitates form during HHT and coarsen with both temperature and holding time, which likely contributes to the ductility loss observed in Fig. 10. Although spatial distribution was not investigated in this study, clustering during HHT may further promote ductility degradation. Finally, porosity of the tensile samples presented in Fig. 10 was not measured, but it should be considered in future work as a possible factor influencing ductility.

As explained earlier, a holding time of 10 min is sufficient to reach a densification plateau at both 540 and 400 °C (see Fig. 8). Fig. 10a shows that the strength loss after HHT at 520 °C remains limited, and Fig. 10b indicates that this decrease is similarly limited after a 10 min HHT. These results suggest that effective healing, while preserving mechanical properties, can be achieved with a 10 min HHT at 520 °C or lower.

4. Conclusion

In this work, a new Al–Mg–Zr alloy, named Almazium®, was successfully developed and processed by PBF-LB/M. The alloy combines a high Mg content with Zr induced grain refinement, resulting in a

fine bimodal microstructure and a yield strength of 317 MPa in the AB condition, more than twice that of PBF-LB/M-processed AlMg8.

The healing ability of Almazium® was demonstrated through both HHT and HHPT treatments. X-ray nano-CT showed that up to 65 % of voids below 1 µm were completely healed after a 30 min HHT at 540 °C, while HHPT enabled complete healing of voids up to at least 100 µm in equivalent diameter. Healing was predominantly attributed to Mg diffusion assisted by vacancies and dislocations, enhanced under applied pressure, and was shown to be repeatable through at least two cycles. While the defect populations involved in the first and second healing cycles are not directly comparable, the results demonstrate the persistence of predominantly diffusion-driven healing after prior healing and subsequent mechanical damage.

Mechanical tests and healing results showed that a compromise between healing and strength could be found by limiting the time of the healing treatment to 10 min and keeping a temperature lower than 480 °C.

Overall, Almazium® demonstrates that a high-strength aluminium alloy can exhibit intrinsic, repeatable healing ability when processed by PBF-LB/M. These results open new pathways for the design of healable aluminium alloys and provide a foundation for developing next-generation lightweight structural materials with extended service life.

CRediT authorship contribution statement

Sophie De Raedemacker: Writing – original draft, Visualization, Validation, Methodology, Investigation, Funding acquisition, Formal analysis, Conceptualization. **Julie Gheysen:** Writing – review & editing, Investigation, Conceptualization. **Florent Hannard:** Writing – review & editing, Supervision, Investigation, Conceptualization. **Julie Villanova:** Writing – review & editing, Resources, Methodology, Investigation, Conceptualization. **William Mottay:** Writing – review & editing, Visualization, Validation, Methodology, Investigation, Conceptualization. **David Tingaud:** Writing – review & editing, Resources, Conceptualization. **Bartłomiej Winiarski:** Writing – review & editing, Methodology, Investigation, Conceptualization. **Masoud Ahmadi:** Writing – review & editing, Visualization, Investigation. **Mohammed Farag:** Writing – review & editing, Visualization, Investigation. **Hosni Idrissi:** Writing – review & editing, Supervision, Conceptualization. **Khalid Hoummada:** Writing – review & editing, Resources, Conceptualization. **Moataz M. Attallah:** Writing – review & editing, Resources, Conceptualization. **Aude Simar:** Writing – review & editing, Supervision, Resources, Project administration, Methodology, Funding acquisition, Conceptualization.

Declaration of generative AI and AI-assisted technologies in the writing process

The authors used ChatGPT in order to improve readability and language of the present manuscript. After using this tool, the authors reviewed and edited the content as needed and take full responsibility for the content of the publication.

Funding

Sophie De Raedemacker is a FRIA grantee of the Fonds National de la Recherche Scientifique - FNRS and gratefully acknowledges their support. Project HAMAAC was selected in the Joint Transnational Call 2022 of M-ERA.NET 3, which is an EU-funded network of about 49 funding organisations (Horizon 2020 grant agreement No. 958174). The project is funded by the Service public de Wallonie SPW - Belgium, Technology Agency of the Czech Republic (TACR) and Région Nouvelle-Aquitaine (RNAQ), France. Avizo software acquisition was supported by the Fonds de la Recherche Scientifique – FNRS - EQP under grant UN06920F. The authors acknowledge the financial support from the European Funds for Regional Development (FEDER) and the Walloon Region in the framework of the operational program “Wallonie-2020.EU” (project: IAWATHA/AManUMater, n°101628-722943) for the acquisition of the X-ray microtomography equipment. This work was also supported by the Fonds de la Recherche Scientifique - FNRS under Grant(s) n° T.0209.23 (PDR - 3D HIPHeal project). The publication was supported by the Fondation Universitaire de Belgique.

Declaration of competing interest

The authors declare the following financial interests/personal relationships which may be considered as potential competing interests:

Aude Simar reports that financial support was provided by Fund for Scientific Research. Aude Simar also reports that financial support was provided by M-ERA.NET. Sophie De Raedemacker has patent pending with Université catholique de Louvain. If there are other authors, they declare that they have no known competing financial interests or personal relationships that could have appeared to influence the work reported in this paper.

Acknowledgements

The authors acknowledge the European Synchrotron Radiation Facility for provision of synchrotron radiation facilities (proposal MA5725) and we would like to thank Grzegorz Pyka, Nicolas Nothomb and Héctor Sepúlveda for assistance in using beamline ID16B and for fruitful discussions. The authors thank the LACAMI platform and LEMSC platform of iMMC/UCLouvain for their technical support and expertise. In particular, Armand Béché for supporting STEM/EDX, Alban Maton for machining tensile samples, Bruno Dell’Aquila for encapsulating the samples prior to heat treatments and Quentin Mestrez for mechanical testing. The support by the Université Sorbonne Paris Nord (USPN) “CARAMEL” platform facility funded by Région Île-de-France and the CNRS for the HIP post-treatments is greatly appreciated. The authors acknowledge Marie-Noëlle Avettand-Fènoël for the discussion about the nature of the observed network.

Appendix A. Supplementary data

Supplementary data to this article can be found online at doi:10.1016/j.matdes.2026.116546.

Data availability

Data will be made available on request.

References

[1] S.C. Altıparmak, V.A. Yardley, Z. Shi, J. Lin, Challenges in additive manufacturing of high-strength aluminium alloys and current developments in hybrid additive manufacturing, Int. J. Lightweight Mater. Manuf. 4 (2) (Jun 2021) 246–261, https://doi.org/10.1016/j.ijlmm.2020.12.004

[2] S.L. Sing, W.Y. Yeong, Laser powder bed fusion for metal additive manufacturing: perspectives on recent developments, Virtual Phys. Prototyp. 15 (3) (Jul 2020) 359–370, https://doi.org/10.1080/17452759.2020.1779999

[3] J. Zhang, J. Gao, B. Song, L. Zhang, C. Han, C. Cai, K. Zhou, Y. Shi, A novel crack-free Ti-modified al-cu-mg alloy designed for selective laser melting, Addit. Manuf. 38 (Feb 2021) 101829, https://doi.org/10.1016/j.addma.2020.101829

[4] H. Zhang, H. Zhu, T. Qi, Z. Hu, X. Zeng, Selective laser melting of high strength al–cu–mg alloys: processing, microstructure and mechanical properties, Mater. Sci. Eng. A 656 (Feb 2016) 47–54, https://doi.org/10.1016/j.msea.2015.12.101

[5] A.B. Spierings, K. Dawson, T. Heeling, P.J. Uggowitzer, R. Schäublin, F. Palm, K. Wegener, Microstructural features of SC- and zr-modified al-mg alloys processed by selective laser melting, Mater Des. 115 (Feb 2017) 52–63, https://doi.org/10.1016/j.matdes.2016.11.040

[6] H. Zhang, H. Zhu, X. Nie, J. Yin, Z. Hu, X. Zeng, Effect of zirconium addition on crack, microstructure and mechanical behavior of selective laser melted al-cu-mg alloy, Scr. Mater. 134 (Jun 2017) 6–10, https://doi.org/10.1016/j.scriptamat.2017.02.036

[7] X. Li, Y. Liu, Microstructure characterization and mechanical performance of laser powder bed fusion processed AlMgScZr alloy: effect of heat treatment, Mater. Sci. Eng. A 862 (Jan 2023) 144501, https://doi.org/10.1016/j.msea.2022.144501

[8] D. Li, J. Liu, N. Zhong, S. Li, Effect of ER addition on the microstructure, mechanical properties and fatigue crack growth behavior of Al-Zn-Mg-Cu alloy fabricated by laser powder bed fusion, Mater. Charact. 237 (Jul 2026) 116487, https://doi.org/10.1016/j.matchar.2026.116487

[9] Y. Chen, D. Zhang, P. O’Toole, D. Qiu, M. Seibold, K. Schricker, J.-P. Bergmann, A. Rack, M. Easton, In situ observation and reduction of hot-cracks in laser additive manufacturing, Commun. Mater. 5 (1) (May 2024) 84, https://doi.org/10.1038/s43246-024-00522-3

[10] S.A. Mantri, T. Ingale, X. Xu, A. Sharma, K.P. Davidson, M.S.K.K.Y. Nartu, S.S. Varahabatla, N.B. Dahotre, R.V. Ramanujan, R. Banerjee, Enhancing printability of titanium aluminides using laser powder bed fusion by exploiting an in-situ massive phase transformation, Addit. Manuf. 115 (Jan 2026) 105067, https://doi.org/10.1016/j.addma.2025.105067

[11] A. Mauduit, S. Pillot, H. Gransac, Study of the suitability of aluminium alloys for additive manufacturing by laser powder bed fusion, U.P.B. Sci. Bull, Series B 79 (2017) 219–238.

[12] D. Herzog, V. Seyda, E. Wycisk, C. Emmelmann, Additive manufacturing of metals, Acta Mater. 117 (Sep 2016) 371–392, https://doi.org/10.1016/j.actamat.2016.07.019

[13] N. Nothomb, I. Rodriguez-Barber, M.T. Pérez-Prado, N.J. Mena, G. Pyka, A. Simar, Understanding the effect of pre-sintering scanning strategy on the relative density of zr-modified Al7075 processed by laser powder bed fusion, Addit. Manuf. Lett. 11 (Dec 2024) 100253, https://doi.org/10.1016/j.addlet.2024.100253

[14] N. Nothomb, I. Rodriguez-Barber, M.-N. Avettand-Fénoël, M.T. Pérez Prado, M. Marinova, A. Simar, Understanding the effect of tailored heat treatment on zr-modified Al7075 fabricated by laser powder bed fusion, Mater Des. 258 (Oct 2025) 114553, https://doi.org/10.1016/j.matdes.2025.114553

[15] J. Gheysen, D. Tingaud, J. Villanova, A. Hocini, A. Simar, Exceptional fatigue life and ductility of new liquid healing hot isostatic pressing especially tailored for additive manufactured aluminum alloys, Scr. Mater. 233 (Aug 2023) 115512, https://doi.org/10.1016/j.scriptamat.2023.115512

[16] J. Gheysen, G. Pyka, B. Winiarski, J. Villanova, F. Hannard, S. De Raedemacker, J. Donoghue, A. Smith, A. Simar, Development and characterisation of a liquid phase assisted healable aluminium-magnesium alloy processed by laser powder bed fusion, Mater Des. (Aug 2025) 114573, https://doi.org/10.1016/j.matdes.2025.114573

[17] J. Gheysen, A. Kashiwar, H. Idrissi, J. Villanova, A. Simar, Suppressing hydrogen blistering in a magnesium-rich healable laser powder bed fusion aluminum alloy analyzed by in-situ high resolution techniques, Mater Des. 231 (Jul 2023) 112024, https://doi.org/10.1016/j.matdes.2023.112024

[18] M. Zhu, J. Wang, T. Wen, Z. He, X. Dong, D. Qiu, S. Ji, Y. Wang, H. Yang, Processability improvement and strength enhancement in laser powder bed fusion of AlMgZr and AlMgZr-Ti alloys, Virtual Phys. Prototyp. 20 (1) (Dec 2025) e2523546, https://doi.org/10.1080/17452759.2025.2523546

[19] Z. Shu, Y. Liu, Microstructure and mechanical properties of a novel Al-Mg-Sc-Ti alloy fabricated by laser powder bed fusion, Materials 17 (3) (Jan 2024) 686, https://doi.org/10.3390/ma17030686

[20] F. Belelli, R. Casati, F. Larini, M. Riccio, M. Vedani, Investigation on two Ti–B-reinforced al alloys for laser powder bed fusion, Mater. Sci. Eng. A 808 (Mar 2021) 140944, https://doi.org/10.1016/j.msea.2021.140944

[21] Y.K. Xiao, Q. Yang, Z.Y. Bian, H. Chen, Y. Wu, Q. Lian, Z. Chen, H.W. Wang, Microstructure, heat treatment and mechanical properties of TiB2/Al–7Si–cu–mg alloy fabricated by selective laser melting, Mater. Sci. Eng. A 809 (Mar 2021) 140951, https://doi.org/10.1016/j.msea.2021.140951

[22] M.F. Khan, R. Ghiaasiaan, P.R. Gradl, S. Shao, N. Shamsaei, Additively manufactured scalmalloy via laser powder bed fusion (L-PBF): temperature-dependent tensile and fatigue behaviors, Fatigue. Fract. Eng. Mat. Struct. 48 (4) (Apr 2025) 1496–1513, https://doi.org/10.1111/ffe.14549

[23] C. Van Der Rest, S. De Raedemacker, M.-N. Avettand-Fènoël, G. Pyka, R. Cocle, A. Simar, Improving the fatigue life of laser powder bed fusion scalmalloy® by friction stir processing, Mater. Des. 244 (Aug 2024) 113193, https://doi.org/10.1016/j.matdes.2024.113193

[24] X. Nie, H. Zhang, H. Zhu, Z. Hu, L. Ke, X. Zeng, Effect of zr content on formability, microstructure and mechanical properties of selective laser melted zr modified Al-4.24Cu-1.97Mg-0.56MN alloys, J. Alloys Compd. 764 (Oct 2018) 977–986, https://doi.org/10.1016/j.jallcom.2018.06.032

[25] J.H. Martin, B.D. Yahata, J.M. Hundley, J.A. Mayer, T.A. Schaedler, T.M. Pollock, 3D printing of high-strength aluminium alloys, Nat. 549 (7672) (Sep 2017) 365–369, https://doi.org/10.1038/nature23894

[26] L. Zhou, H. Hyer, S. Park, H. Pan, Y. Bai, K.P. Rice, Y. Sohn, Microstructure and mechanical properties of zr-modified aluminum alloy 5083 manufactured by laser powder bed fusion, Addit. Manuf. 28 (Aug 2019) 485–496, https://doi.org/10.1016/j.addma.2019.05.027

[27] A.P. Mouritz, Aluminium alloys for aircraft structures, in: Introduction to Aerospace Materials, Woodhead Publishing, 2012, pp. 173–201, https://doi.org/10.1533/9780857095152.173. Elsevier.

[28] J.R. Croteau, S. Griffiths, M.D. Rossell, C. Leinenbach, C. Kenel, V. Jansen, D.N. Seidman, D.C. Dunand, N.Q. Vo, Microstructure and mechanical properties of al-mg-zr alloys processed by selective laser melting, Acta Mater. 153 (Jul 2018) 35–44, https://doi.org/10.1016/j.actamat.2018.04.053

[29] K.V. Yang, P. Rometsch, T. Jarvis, J. Rao, S. Cao, C. Davies, X. Wu, Porosity formation mechanisms and fatigue response in Al-Si-Mg alloys made by selective laser melting, Mater. Sci. Eng. A 712 (Jan 2018) 166–174, https://doi.org/10.1016/j.msea.2017.11.078

[30] J.G. Santos Macías, L. Zhao, D. Tingaud, B. Bacroix, G. Pyka, C. Van Der Rest, L. Ryelandt, A. Simar, Hot isostatic pressing of laser powder bed fusion AlSi10Mg: parameter identification and mechanical properties, J. Mater. Sci. 57 (21) (Jun 2022) 9726–9740, https://doi.org/10.1007/s10853-022-07027-9

[31] J.G. Santos Macías, C. Elangeswaran, L. Zhao, J.-Y. Buffière, B. Van Hooreweder, A. Simar, Fatigue crack nucleation and growth in laser powder bed fusion AlSi10Mg under as built and post-treated conditions, Mater Des. 210 (Nov 2021) 110084, https://doi.org/10.1016/j.matdes.2021.110084

[32] S.R. White, N.R. Sottos, P.H. Geubelle, J.S. Moore, M.R. Kessler, S.R. Sriram, E.N. Brown, S. Viswanathan, Autonomic healing of polymer composites, Nat. 409 (6822) (Feb 2001) 794–797, https://doi.org/10.1038/35057232

[33] S. Bode, M. Enke, M. Hernandez, R.K. Bose, A.M. Grande, S. Van Der Zwaag, U.S. Schubert, S.J. Garcia, M.D. Hager, Characterization of self-healing polymers: from macroscopic healing tests to the molecular mechanism, In M.D. Hager, S. Van Der Zwaag, U.S. Schubert (Eds.), Self-Healing Materials, vol. 273, Springer International Publishing, Cham, 2015, pp. 113–142, https://doi.org/10.1007/12_2015_341

[34] N. Van Dijk, S. Van Der Zwaag, Self-healing phenomena in metals, Adv. Mater. Interfaces 5 (17) (Sep 2018) 1800226, https://doi.org/10.1002/admi.201800226

[35] M. Arseenko, J. Gheysen, F. Hannard, N. Nothomb, A. Simar, Self-healing in metal-based systems, In A. Kanellopoulos, J. Norambuena-Contreras (Eds.), Self-Healing Construction Materials, Springer International Publishing, Cham, 2022, pp. 43–78, https://doi.org/10.1007/978-3-030-86880-2_3

[36] K.K. Alaneme, M.O. Bodunrin, Self-healing using metallic material systems – a review, Appl. Mater. Today 6 (Mar 2017) 9–15, https://doi.org/10.1016/j.apmt.2016.11.002

[37] M. Arseenko, F. Hannard, L. Ding, L. Zhao, E. Maire, J. Villanova, H. Idrissi, A. Simar, A new healing strategy for metals: programmed damage and repair, Acta Mater. 238 (Oct 2022) 118241, https://doi.org/10.1016/j.actamat.2022.118241

[38] M. Song, K. Du, S.P. Wen, Z.R. Nie, H.Q. Ye, In situ electron microscopy investigation of void healing in an Al–Mg–Er alloy at a low temperature, Acta Mater. 69 (May 2014) 236–245, https://doi.org/10.1016/j.actamat.2014.02.004

[39] J.T. Kim, H.J. Kim, S.H. Hong, H.J. Park, Y.S. Kim, Y.J. Hwang, Y.B. Jeong, J.-Y. Park, J.M. Park, B. Sarac, W.-M. Wang, J. Eckert, K.B. Kim, Thermally-triggered dual in-situ self-healing metallic materials, Sci. Rep. 8 (1) (Feb 2018) 2120, https://doi.org/10.1038/s41598-018-19936-4

[40] G. Siroky, E. Kraker, J. Rosc, D. Kieslinger, R. Brunner, S. Van Der Zwaag, E. Kozeschnik, W. Ecker, Analysis of Sn-Bi solders: X-ray micro computed tomography imaging and microstructure characterization in relation to properties and liquid phase healing potential, Materials 14 (1) (Dec 2020) 153, https://doi.org/10.3390/ma14010153

[41] X. Hu, C. Guo, Y. Huang, Z. Xu, Z. Shi, F. Zhou, G. Li, Y. Zhou, Y. Li, Z. Li, Z. Li, H. Lu, H. Ding, H. Dong, Q. Zhu, Liquid-induced healing of cracks in nickel-based superalloy fabricated by laser powder bed fusion, Acta Mater. 267 (Apr 2024) 119731, https://doi.org/10.1016/j.actamat.2024.119731

[42] H. Yu, J. Shao, S. Shuai, C. Chen, L. Wang, D. San-Martín, W. Xu, The application of self-healing concept in ni superalloys: theoretical design and experimental validation, Mater. Des. (Dec 2023) 112587, https://doi.org/10.1016/j.matdes.2023.112587

[43] F. Czerwinski, Thermal stability of aluminum alloys, Materials 13 (15) (Aug 2020) 3441, https://doi.org/10.3390/ma13153441

[44] M. Akshansh, Friction stir welding of dissimilar metal: a review, Int. J. Res. Appl. Sci. Eng. Technol. 6 (Jan 2018) 1551–1559, https://doi.org/10.22214/ijraset.2018.13032

[45] S. Zhang, J. Kohlbrecher, F.D. Tichelaar, G. Langelaan, E. Brück, S. Van Der Zwaag, N.H. Van Dijk, Defect-induced au precipitation in FE–au and FE–au–B–N alloys studied by in situ small-angle neutron scattering, Acta Mater. 61 (18) (Oct 2013) 7009–7019, https://doi.org/10.1016/j.actamat.2013.08.015

[46] C.H. Suresh, N. Koga, A consistent approach toward atomic radii, J. Phys. Chem. A 105 (24) (Jun 2001) 5940–5944, https://doi.org/10.1021/jp010432b

[47] M. Van Rooyen, J.A.S. Maartensdijk, E.J. Mittemeijer, Precipitation of guinier-Preston zones in aluminum- magnesium; a calorimetric analysis of liquid-quenched and solid-quenched alloys, Metall. Trans. A. 19 (10) (Oct 1988) 2433–2443, https://doi.org/10.1007/BF02645471

[48] H. Fu, H. Yan, B. Wei, B. Sun, Z. Liu, W. Gao, Effect of zr additions on the microstructure and elevated-temperature mechanical properties of Al–Cu–Mg–Ag–Zn–Mn–Zr alloys, Materials 18 (17) (Aug 2025) 4062, https://doi.org/10.3390/ma18174062

[49] P. Bidare, I. Bitharas, R.M. Ward, M.M. Attallah, A.J. Moore, Laser powder bed fusion in high-pressure atmospheres, Int. J. Adv. Manuf. Technol. 99 (1–4) (Oct 2018) 543–555, https://doi.org/10.1007/s00170-018-2495-7

[50] G. Shi, R. Zhang, Y. Cao, G. Yang, A review of the vaporization behavior of some metal elements in the LPBF process, Micromachines 15 (7) (Jun 2024) 846, https://doi.org/10.3390/mi15070846

[51] L. Deillon, F. Jensch, F. Palm, M. Bambach, A new high strength Al–Mg–Sc alloy for laser powder bed fusion with calcium addition to effectively prevent magnesium evaporation, J. Mater. Process. Technol. 300 (Feb 2022) 117416, https://doi.org/10.1016/j.jmatprotec.2021.117416

[52] M.A. Al-Hashem, R.K. Gupta, Corrosion behavior of high-strength aluminum alloys produced by laser powder bed fusion: a critical review, J. Alloys Compd. 1065 (May 2026) 188054, https://doi.org/10.1016/j.jallcom.2026.188054

[53] J.-J. Fundenberger, B. Beausir, ATEX - analysis tools for electron and X-ray diffraction, http://www.atex-software.eu/.

[54] D.J. Larson, T.J. Prosa, R.M. Ulfig, B.P. Geiser, T.F. Kelly, Local Electrode Atom Probe Tomography: A User's Guide, Springer New York, New York, NY, 2013, https://link.springer.com/10.1007/978-1-4614-8721-0.

[55] J.-O. Andersson, T. Helander, L. Höglund, P. Shi, B. Sundman, Thermo-calc & DICTRA, computational tools for materials science, CALPHAD 26 (2) (Jun 2002) 273–312, https://doi.org/10.1016/S0364-5916(02)00037-8

[56] S. De Raedemacker, J. Gheysen, F. Hannard, N. Nothomb, G. Pyka, H. Sepúlveda, A. Simar, Investigation by 3D nano-imaging of the multiple healing ability and kinetics of new 3D printed high strength Al alloys [Dataset]. European Synchrotron Radiation Facility, 2026, https://doi.org/10.15151/ESRF-ES-1108356214.

[57] A. Mirone, E. Brun, E. Gouillart, P. Tafforeau, J. Kieffer, The PyHST2 hybrid distributed code for high speed tomographic reconstruction with iterative reconstruction and a priori knowledge capabilities, Nucl. Instrum. Methods Phys. Res, B 324 (Apr 2014) 41–48, https://doi.org/10.1016/j.nimb.2013.09.030

[58] J. Gheysen, Design, Development and Characterisation of New Healable Aluminium Alloys for Laser Powder Bed Fusion (Ph.D. thesis), Université Catholique de Louvain, 2022, http://hdl.handle.net/2078.1/271186.
[59] B. Winiarski, J. Gheysen, G. Pyka, F. Hannard, M. Arseenko, J. Villanova, A. Brinek, A. Chirazi, L. Jiang, A. Simar, Correlative microscopy discovers self-healing of AM-build al-mg alloy, Microsc. Microanal. 29 (Supplement_1) (Jul 2023) 1981–1982, https://doi.org/10.1093/micmic/ozad067.1026
[60] K. Knipling, Precipitation evolution in al–zr and Al–Zr–Ti alloys during aging at 450–600°C, Acta Mater. 56 (6) (Apr 2008) 1182–1195, https://doi.org/10.1016/j.actamat.2007.11.011
[61] F. Larini, R. Casati, S. Marola, C. Andrianopoli, P. Bajaj, M. Vedani, Effect of combined additions of SC, zr and Ti on hot-cracking resistance and precipitation behaviour in al-mg alloy by L-PBF, Materialia 35 (Jun 2024) 102127, https://doi.org/10.1016/j.mtla.2024.102127
[62] S. Griffiths, M.D. Rossell, J. Croteau, N.Q. Vo, D.C. Dunand, C. Leinenbach, Effect of laser rescanning on the grain microstructure of a selective laser melted al-mg-zr alloy, Mater. Charact. 143 (Sep 2018) 34–42, https://doi.org/10.1016/j.matchar.2018.03.033
[63] R. Xu, R. Li, T. Yuan, H. Zhu, M. Wang, J. Li, W. Zhang, P. Cao, Laser powder bed fusion of al–mg–zr alloy: microstructure, mechanical properties and dynamic precipitation, Mater. Sci. Eng. A 859 (Nov 2022) 144181, https://doi.org/10.1016/j.msea.2022.144181
[64] L.S. Toth, S. Biswas, C. Gu, B. Beausir, Notes on representing grain size distributions obtained by electron backscatter diffraction, Mater. Charact. 84 (Oct 2013) 67–71, https://doi.org/10.1016/j.matchar.2013.07.013
[65] S. Griffiths, J.R. Croteau, M.D. Rossell, R. Erni, A. De Luca, N.Q. Vo, D.C. Dunand, C. Leinenbach, Coarsening- and creep resistance of precipitation-strengthened al–mg–zr alloys processed by selective laser melting, Acta Mater. 188 (Apr 2020) 192–202, https://doi.org/10.1016/j.actamat.2020.02.008
[66] R. Lumley, Self healing in aluminium alloys, In R. Hull, R.M.O. Jr, J. Parisi, H. Warlimont, S. Van Der Zwaag (Eds.), Self Healing Materials, vol. 100, Springer Netherlands, Dordrecht, 2007, pp. 219–254, https://doi.org/10.1007/978-1-4020-6250-6_11
[67] S. Zhou, Z. Zhang, M. Li, D. Pan, H. Su, X. Du, P. Li, Y. Wu, Effect of SC on microstructure and mechanical properties of as-cast al–mg alloys, Mater Des. 90 (Jan 2016) 1077–1084, https://doi.org/10.1016/j.matdes.2015.10.132
[68] D. Pan, S. Zhou, Z. Zhang, M. Li, Y. Wu, Effects of SC(zr) on the microstructure and mechanical properties of as-cast al–mg alloys, Mater. Sci. Eng. A 33 (6) (Apr 2017) 751–757, https://doi.org/10.1080/02670836.2016.1270573
[69] M. Schuster, A. De Luca, A. Mathur, E. Hosseini, C. Leinenbach, Precipitation in a 2XXX series al-cu-mg-zr alloy fabricated by laser powder bed fusion, Mater Des. 211 (Dec 2021) 110131, https://doi.org/10.1016/j.matdes.2021.110131
[70] Y. Chen, X. Chen, H. Chen, Y. Xiao, J. Dai, Y. Chen, Y. Cui, C. Dan, Z. Chen, X. Li, H. Wang, Abnormal grain growth in randomly-oriented fine grains in an Al–Mg–Sc–Zr alloy processed by laser-powder-bed-fusion, Mater. Res. Lett. 12 (9) (Sep 2024) 635–643, https://doi.org/10.1080/21663831.2024.2366878
[71] A. Aversa, G. Marchese, A. Saboori, E. Bassini, D. Manfredi, S. Biamino, D. Ugues, P. Fino, M. Lombardi, New aluminum alloys specifically designed for laser powder bed fusion: a review, Materials 12 (7) (Mar 2019) 1007, https://doi.org/10.3390/ma12071007
[72] W. Mottay, Mécanismes élémentaires Du Vieillissement Sous Déformation de Soudures En Acier C-Mn Du Circuit Secondaire de L'epr, 2024, https://doi.org/10.13140/RG.2.2.30590.80966
[73] Q. Lin, S.J. Neethling, K.J. Dobson, L. Courtois, P.D. Lee, Quantifying and minimising systematic and random errors in X-ray micro-tomography based volume measurements, Comput. Geosci. 77 (Apr 2015) 1–7, https://doi.org/10.1016/j.cageo.2014.12.008
[74] J. Fiocchi, A. Tuissi, C.A. Biffi, Heat treatment of aluminium alloys produced by laser powder bed fusion: a review, Mater Des. 204 (Jun 2021) 109651, https://doi.org/10.1016/j.matdes.2021.109651
[75] X. Sauvage, A. Ganeev, Y. Ivanisenko, N. Enikeev, M. Murashkin, R. Valiev, Grain boundary segregation in UFG alloys processed by severe plastic deformation, Adv. Eng. Mater. 14 (11) (Nov 2012) 968–974, https://doi.org/10.1002/adem.201200060
[76] R. Goswami, P.S. Pao, S.B. Qadri, R.L. Holtz, Severe plastic deformation induced sensitization of cryo-milled nanocrystalline Al-7.5 mg, Metall. Mater. Trans. A 45 (6) (Jun 2014) 2894–2898, https://doi.org/10.1007/s11661-014-2227-z
[77] S.-J.L. Kang (editor), Sintering: Densification, Grain Growth, and Microstructure, Elsevier Butterworth-Heinemann, Amsterdam Boston London, 2005.
[78] P.E. Leser, J.A. Newman, S.W. Smith, W.P. Leser, R.A. Wincheski, T.A. Wallace, E.H. Glaessgen, R.S. Piascik, Mitigation of Crack Damage in Metallic Materials. Technical report, National Aeronautics and Space Administration, Langley Research Center, May 2014.
[79] B. Grabowski, C.C. Tasan, Self-healing metals, In M.D. Hager, S. Van Der Zwaag, U.S. Schubert (Eds.), Self-Healing Materials, vol. 273, Springer International Publishing, Cham, 2016, pp. 387–407, https://doi.org/10.1007/12_2015_337
[80] C.B. Finfrock, A. Exil, J.D. Carroll, L. Deibler, Effect of hot isostatic pressing and powder feedstock on porosity, microstructure, and mechanical properties of selective laser melted AlSi10Mg, Metallogr. Microstruct. Anal. 7 (4) (Aug 2018) 443–456, https://doi.org/10.1007/s13632-018-0456-z
[81] J.P. Oliveira, A.D. LaLonde, J. Ma, Processing parameters in laser powder bed fusion metal additive manufacturing, Mater. Des. 193 (Aug 2020) 108762, https://doi.org/10.1016/j.matdes.2020.108762
[82] H.R. Kotadia, G. Gibbons, A. Das, P.D. Howes, A review of laser powder bed fusion additive manufacturing of aluminium alloys: microstructure and properties, Addit. Manuf. 46 (Oct 2021) 102155, https://doi.org/10.1016/j.addma.2021.102155
[83] L. Dowling, J. Kennedy, S. O'Shaughnessy, D. Trimble, A review of critical repeatability and reproducibility issues in powder bed fusion, Mater. Des. 186 (Jan 2020) 108346, https://doi.org/10.1016/j.matdes.2019.108346
[84] E.L. Huskins, B. Cao, K.T. Ramesh, Strengthening mechanisms in an al–mg alloy, Mater. Sci. Eng. A 527 (6) (Mar 2010) 1292–1298, https://doi.org/10.1016/j.msea.2009.11.056
[85] S.I. Shakil, W. Bednarczyk, M. Gajewska, Z. Mahbooba, A. Saharan, A. Tridello, D.S. Paolino, M. Haghshenas, Microstructure and very high cycle fatigue characteristics of powder bed fused – laser beam (PBF-LB) scandium-free al-mg-zr alloy, Mater. Sci. Eng. A 930 (May 2025) 148177, https://doi.org/10.1016/j.msea.2025.148177
[86] Bruker Nano GmbH, Introduction to EDS Analysis - Reference Manual, 2011.
[87] Y.F. Gao, W. Zhang, P.J. Shi, W.L. Ren, Y.B. Zhong, A mechanistic interpretation of the strength-ductility trade-off and synergy in lamellar microstructures, Mater. Today Adv. 8 (Dec 2020) 100103, https://doi.org/10.1016/j.mtadv.2020.100103
[88] D. Witkin, Z. Lee, R. Rodriguez, S. Nutt, E. Lavernia, Al–mg alloy engineered with bimodal grain size for high strength and increased ductility, Scr. Mater. 49 (4) (Aug 2003) 297–302, https://doi.org/10.1016/S1359-6462(03)00283-5
[89] P. Rodriguez, Serrated plastic flow, Bull. Mater. Sci. 6 (4) (Sep 1984) 653–663, https://doi.org/10.1007/BF02743993
[90] W. Mottay, D. Caillard, H. Idrissi, P. Maugis, A. Portavoce, F. Roch, C. Perrin-Pellegrino, K. Hoummada, Investigation of the influence of manganese on the dynamic strain ageing of ferritic steels – Part II: Industrial alloy, Acta Mater. 301 (Dec 2025) 121576, https://doi.org/10.1016/j.actamat.2025.121576
[91] T.A. Lebedkina, M.A. Lebyodkin, Effect of deformation geometry on the intermittent plastic flow associated with the Portevin–Le chatelier effect, Acta Mater. 56 (19) (Nov 2008) 5567–5574, https://doi.org/10.1016/j.actamat.2008.07.025
[92] G. Saad, S.A. Fayek, A. Fawzy, H.N. Soliman, E. Nassr, Serrated flow and work hardening characteristics of Al-5356 alloy, J. Alloys Compd. 502 (1) (Jul 2010) 139–146, https://doi.org/10.1016/j.jallcom.2010.04.119
[93] K. Bouabdallah, Caractérisation de L'effet Portevin-Le Chatelier Dans Les Alliages Aluminium Magnésium - Apport Des Techniques D'analyse D'images (Ph.D. thesis), Université de Savoie, Jan 2006, https://theses.hal.science/tel-00193176.
[94] N. Tian, G. Wang, Y. Zhou, K. Liu, G. Zhao, L. Zuo, Study of the Portevin-Le chatelier (PLC) characteristics of a 5083 aluminum alloy sheet in two heat treatment states, Materials 11 (9) (Aug 2018) 1533, https://doi.org/10.3390/ma11091533
[95] F. Hannard, T. Pardoen, E. Maire, C. Le Bourlot, R. Mokso, A. Simar, Characterization and micromechanical modelling of microstructural heterogeneity effects on ductile fracture of 6XXX aluminium alloys, Acta Mater. 103 (Jan 2016) 558–572, https://doi.org/10.1016/j.actamat.2015.10.008